

# 21CMFISH: Fisher-matrix framework for fast parameter forecasts from the cosmic 21-cm signal

Charlotte A. Mason <sup>1,2</sup>★ Julian B. Muñoz,<sup>3,4</sup> Bradley Greig <sup>5,6</sup> Andrei Mesinger <sup>7</sup>  
and Jaehong Park <sup>8</sup>

<sup>1</sup>*Cosmic Dawn Center (DAWN)*

<sup>2</sup>*Niels Bohr Institute, University of Copenhagen, Jagtvej 128, 2200 København N, Denmark*

<sup>3</sup>*Center for Astrophysics | Harvard & Smithsonian, 60 Garden St., Cambridge, MA 02138, USA*

<sup>4</sup>*Department of Astronomy, The University of Texas at Austin, Austin, TX 78712, USA*

<sup>5</sup>*School of Physics, University of Melbourne, Parkville, VIC 3010, Australia*

<sup>6</sup>*ARC Centre of Excellence for All Sky Astrophysics in 3 Dimensions (ASTRO 3D)*

<sup>7</sup>*Scuola Normale Superiore, 56126 Pisa, PI, Italy*

<sup>8</sup>*School of Physics, Korea Institute for Advanced Study (KIAS), 85 Hoegiro, Dongdaemun-gu, Seoul 02455, Republic of Korea*

Accepted 2023 July 9. Received 2023 June 22; in original form 2022 December 16

## ABSTRACT

The 21-cm signal from neutral hydrogen in the early universe will provide unprecedented information about the first stars and galaxies. Extracting this information, however, requires accounting for many unknown astrophysical processes. Seminumerical simulations are key for exploring the vast parameter space of said processes. These simulations use approximate techniques such as excursion-set and perturbation theory to model the 3D evolution of the intergalactic medium, at a fraction of the computational cost of hydrodynamic and/or radiative transfer simulations. However, exploring the enormous parameter space of the first galaxies can still be computationally expensive. Here, we introduce 21CMFISH, a Fisher-matrix wrapper for the seminumerical simulation 21CMFAST. 21CMFISH facilitates efficient parameter forecasts, scaling to significantly higher dimensionalities than MCMC approaches, assuming a multivariate Gaussian posterior. Our method produces comparable parameter uncertainty forecasts to previous MCMC analyses but requires  $\sim 10^4 \times$  fewer simulations. This enables a rapid way to prototype analyses adding new physics and/or additional parameters. We carry out a forecast for HERA using the largest astrophysical parameter space to date, with 10 free parameters, spanning both population II and III star formation. We find X-ray parameters for the first galaxies could be measured to sub-percent precision, and, though they are highly degenerate, the stellar-to-halo mass relation and ionizing photon escape fraction for population II and III galaxies can be constrained to  $\sim 10$  per cent precision (logarithmic quantities). Using a principal component analysis, we find HERA is most sensitive to the product of the ionizing escape fraction and the stellar-to-halo mass fraction for population II galaxies.

**Key words:** galaxies: high-redshift – dark ages, reionization, first stars.

## 1 INTRODUCTION

The cosmic 21-cm signal will soon open a new window on the early universe. The signal is a net absorption or emission of 21-cm photons relative to the cosmic microwave background (CMB) by neutral hydrogen gas in the intergalactic medium (IGM) that depends sensitively on the formation redshift and properties of the universe’s first stars and galaxies, (see e.g. reviews by Furlanetto 2006; Morales & Wythe 2010; Pritchard & Loeb 2012; Mesinger 2019). When the first stars form ( $z \sim 30$ ), their ultraviolet (UV) radiation couples the spin temperature of neutral hydrogen to the cooler kinetic temperature of the gas, via the Wouthuysen–Field effect (e.g. Hirata 2006), driving a net absorption of CMB photons at 21-cm wavelengths. Later, as the galaxy population builds up, X-ray emission from the first galaxies is expected to heat the IGM,

driving the 21-cm signal into emission ( $z \lesssim 15$ ), and eventually, as hydrogen reionizes, the signal decays to zero ( $z \lesssim 10$ ). As the formation redshift and abundance of the first stars is highly sensitive to the build up of low mass dark-matter haloes ( $M_h \sim 10^{6-8} M_\odot$ ) and astrophysical feedback effects which govern star formation, the redshift evolution of the 21-cm signal can be used to constrain astrophysical and cosmological properties in the early universe. This will be an exciting way to see beyond the limits of optical and near-infrared telescopes.

In the coming decade, a number of experiments will reach the expected sensitivity required to measure the 21-cm power spectrum at  $z > 6$ , including e.g. the Hydrogen Epoch of Reionization Array (HERA; DeBoer et al. 2017; The HERA Collaboration et al. 2022b) and the Square Kilometer Array (SKA; Koopmans et al. 2015), while current instruments have set strong upper limits: the Murchison Widefield Array (MWA Tingay et al. 2013; Trott et al. 2020) and the Low Frequency Array (LOFAR; van Haarlem et al. 2013; Gehlot et al. 2019; Mertens et al. 2020), and a claimed first measurement

\* E-mail: [charlotte.mason@nbi.ku.dk](mailto:charlotte.mason@nbi.ku.dk)

of the 21-cm global signal has been made at  $z \sim 18$  (Bowman et al. 2018 though cf. Hills et al. 2018; Singh et al. 2022). To interpret these upcoming data, it is imperative to compare observations to models which encompass as much of the unknown physics of the early universe as possible. In recent years, there has been a particular effort to create parametric models which describe the key astrophysical and cosmological mechanisms which could affect the 21-cm signal (e.g. 21CMFAST<sup>1</sup>; Mesinger & Furlanetto 2007; SIMFAST21; Santos et al. 2010; Visbal & Loeb 2010; Mesinger, Furlanetto & Cen 2011; ZREION; Battaglia et al. 2013; ARES; Mirocha 2014; REIONYUGA; Majumdar et al. 2014; GRIZZLY; Ghara, Choudhury & Datta 2015; SCRITDRAGONS; Mutch et al. 2016; Mondal, Bharadwaj & Majumdar 2017; Choudhury & Paranjape 2018; Murray et al. 2020; ASTRAEUS; Hutter et al. 2021).

Unknown physics in the early universe determines the formation of the first stars and galaxies and the heating and ionization of the IGM which in turn sets the amplitude and spatial structure of the 21-cm signal. For example: the strength of star formation feedback in low-mass haloes; Lyman–Werner feedback; the impact of streaming velocities between baryons and dark matter; the typical X-ray emission of early galaxies; and the escape fraction of hydrogen ionizing photons from galaxies all contribute to the strength of the 21-cm signal via their impact on the formation redshifts and typical bias of the first galaxies, the level of inhomogeneous heating of the IGM during cosmic dawn, and the rate at which hydrogen is reionized (e.g. Muñoz et al. 2022). The degeneracies between some of these effects have been explored (e.g. Park et al. 2019; Qin et al. 2020, 2021a) but due to computational inefficiencies there has not been a thorough investigation of the degeneracies between effects that govern population II and population III star formation. It is furthermore unclear how much the astrophysical effects will hamper our efforts to understand the underlying cosmology: for example, Sitwell et al. (2014), Muñoz, Dvorkin & Cyr-Racine (2020), and Jones et al. (2021) have explored the impact of warm, fuzzy, and self-interacting (ETHOS) dark-matter models on the 21-cm signal, respectively, but did not carry out a full exploration of the degeneracies with astrophysical parameters. Only a few key observables, like the shape of the velocity-induced acoustic oscillations (VAOs; Muñoz 2019b) are immune to astrophysical uncertainties.

Once 21-cm detections are available, one would ideally map out the multidimensional posterior of astrophysics and cosmology using Bayesian inference techniques such as MCMC or Nested sampling (e.g. 21CMC<sup>2</sup>; Greig & Mesinger 2015, 2017). However, mapping out the full posterior is extremely expensive in the high dimensional parameter space of generalized galaxy and cosmological models. Before having a detection, however, decisions on observational strategies, telescope design, synergies, etc. can be guided by much faster (albeit more approximate) forecasting techniques, such as Fisher-matrix analyses<sup>3</sup>

In this paper, we use a Fisher-matrix analysis to explore an unprecedentedly large 21CMFAST astrophysical parameter space. We demonstrate that the Fisher-matrix analysis produces comparable parameter uncertainties to an MCMC with 21CMC (which was

restricted to population II galaxy parameters only), recovering the same degeneracies and very comparable error bars. Having validated our approach, we carry out a Fisher-matrix analysis for the largest parameter set to date in 21CMFAST: 10 free parameters, including both population II and population III galaxies over  $z \sim 5$ –30. Our method reduces the computational cost significantly compared to a typical 21CMC run: requiring a factor  $\sim 10^4$  fewer individual simulations. We carry out a principal component analysis of our Fisher matrix to determine which combinations of parameters will be most easily constrained by observations. We provide a public release of our code 21CMFISH<sup>4</sup>, which is a PYTHON wrapper for 21CMFAST to perform Fisher-matrix analyses.

This approach will enable us to easily add new parameters, e.g. cosmological and dark-matter parameters, to quickly assess how well upcoming 21-cm experiments will be able to constrain them, which will be the topic of a future work (Verwohlt et al. in preparation). The Fisher matrix could also be used for prototyping instrument designs and instrumental noise estimates.

This paper is structured as follows. Section 2 describes our method for generating the 21-cm signal with 21CMFAST, the astrophysical model and our Fisher-matrix formalism in 21CMFISH. Section 3 describes our results of the comparison between the Fisher-matrix analysis and MCMC, and our exploration of the extended model parameter space. We discuss our results in Section 4 and summarize our conclusions in Section 5.

In this work, we fix the cosmological parameters to the best fit from Planck 2018 data (TT,TE,EE + lowE + lensing + BAO from Planck Collaboration VI 2020), and all distances are comoving unless specified otherwise.

## 2 METHODS

Here, we provide a brief overview of the astrophysical model (Section 2.1) and the 21-cm signal (Section 2.2), our Fisher-matrix analysis approach (Section 2.3), and the generation of simulated observations (Section 2.4). The parametric 21CMFAST astrophysical model we use is described by Park et al. (2019), Qin et al. (2020, 2021a, b), and Muñoz et al. (2022) and we refer readers there for more details.

### 2.1 The astrophysical model

We use the public code 21CMFAST (Mesinger & Furlanetto 2007; Mesinger et al. 2011; Murray et al. 2020) to model the 21-cm signal. We use version 3.1.0<sup>5</sup> which includes a parametric model for galaxy formation in both atomic cooling galaxies and molecular cooling galaxies, accounting for all major feedback mechanisms on these galaxies, as well as detailed IGM physics such as inhomogeneous recombinations. The model is fully described by Park et al. (2019), Qin et al. (2020), and Muñoz et al. (2022) and we refer the reader there for more details. Park et al. (2019) describe the halo-mass dependent star formation prescription for population II galaxies, Qin et al. (2020) added a prescription for population III galaxies, and Muñoz et al. (2022) self-consistently included feedback effects on population III star formation – Lyman–Werner feedback and relative velocities between dark matter and baryons. Here, we provide a brief overview of the astrophysical model.

<sup>1</sup><https://github.com/21cmfast/21cmFAST>

<sup>2</sup><https://github.com/21cmfast/21CMC>

<sup>3</sup>Fisher-matrix analyses assume a ‘fiducial’ (i.e. maximum likelihood) parameter set, and computes a multivariate Gaussian posterior around that point. These are reasonable approximations, given that we already have a decent estimate of a ‘fiducial’ model using current data, and previous inference results suggest that the posterior is likely only weakly multimodal/non-Gaussian (e.g. Qin et al. 2021a, b; The HERA Collaboration et al. 2022a).

<sup>4</sup><https://github.com/charlottenosam/21cmfish>

<sup>5</sup><https://github.com/21cmfast/21cmFAST/releases/tag/3.1.0>

As haloes form hierarchically, we assume that the first generation of stars (population III) form out of pristine gas in molecular cooling galaxies, where gas can cool via transitions in  $\text{H}_2$  ( $T_{\text{vir}} \gtrsim 10^3 \text{ K}$ ,  $M_{\text{h}} \gtrsim 10^6 M_{\odot}$ , e.g. Barkana & Loeb 2001), whereas later generations of stars (population II) form in more massive atomic cooling galaxies, where gas cools through atomic transitions ( $T_{\text{vir}} \gtrsim 10^4 \text{ K}$ , corresponding to  $M_{\text{h}} \gtrsim 10^8 M_{\odot}$ ), as haloes grow and the galaxies' ISM is enriched. 21CMFAST models these two galaxy populations separately, as described below. Throughout this work, we use PopII or superscript 'II' to refer to atomic cooling galaxies with population II stars, and PopIII or superscript 'III' to refer to molecular cooling galaxies with population III stars.

The number densities of these galaxies are given by:

$$\frac{dn_{\text{g}}}{dM_{\text{h}}} = \frac{dn}{dM_{\text{h}}} \times f_{\text{duty}}(M_{\text{h}}), \quad (1)$$

where  $\frac{dn}{dM_{\text{h}}}$  is the halo mass function<sup>6</sup>, and  $f_{\text{duty}}$  accounts for the suppression of galaxy formation in haloes below a certain mass scale due to a combination of cooling and feedback processes:

$$f_{\text{duty}} = \begin{cases} \exp\left(-\frac{M_{\text{turn}}^{\text{II}}}{M_{\text{h}}}\right) & \text{PopII} \\ \exp\left(-\frac{M_{\text{turn}}^{\text{III}}}{M_{\text{h}}}\right) \exp\left(-\frac{M_{\text{h}}}{M_{\text{atom}}}\right) & \text{PopIII.} \end{cases} \quad (2)$$

Here, the second term for population III galaxies produces a smooth transition between the two galaxy populations. The characteristic mass scales where galaxy formation is suppressed,  $M_{\text{turn}}^{\text{II}}$ ,  $M_{\text{turn}}^{\text{III}}$ , may be set as a free parameter to be inferred (e.g. Park et al. 2019) or modelled physically as a function of redshift and local radiative background strength (e.g. Muñoz et al. 2022).

For population II atomic cooling galaxies, the suppression is determined by atomic cooling and photoionization feedback, and has a characteristic mass scale

$$M_{\text{turn}}^{\text{II}} = \max[M_{\text{atom}}, M_{\text{ion}}] \quad (3)$$

where  $M_{\text{atom}}$  is the minimum mass scale of atomic cooling (corresponding to a virial temperature of  $\sim 10^4 \text{ K}$ , e.g. Barkana & Loeb 2001; Oh & Haiman 2002),  $M_{\text{ion}}$  is the mass scale where photoheating feedback from inhomogeneous reionization becomes important (e.g. Sobacchi & Mesinger 2014).

For molecular cooling population III galaxies, in addition to the photoionization feedback, we follow Muñoz et al. (2022) (see also Fialkov et al. 2013; Muñoz 2019a) and include the two dominant sources of feedback that reduce the efficiency of star formation in molecular cooling haloes: (i) Lyman–Werner feedback, due to stellar emission at 11.2–13.6 eV which effectively photodissociates molecular hydrogen, stalling the cooling of gas in population III galaxies and thus impeding star formation; and (ii) dark matter–baryon streaming velocities which reduce the accretion of gas into dark-matter haloes, which both slows the formation of haloes, due to the lower gravitational potential, and reduces the gas available to form stars.

The strength of these two effects depends on the Lyman–Werner background flux ( $J_{21}$ , in units  $10^{-21} \text{ erg s}^{-1} \text{ cm}^{-2} \text{ Hz}^{-1} \text{ sr}^{-1}$ ) and the relative velocity between dark matter and baryons ( $v_{\text{cb}}$  in  $\text{km s}^{-1}$ ) as a function of redshift. Therefore,

$$M_{\text{turn}}^{\text{III}} = \max[M_{\text{mol}}, M_{\text{ion}}], \quad (4)$$

where we use the parametrization of Muñoz et al. (2022)

$$M_{\text{mol}}(z, v_{\text{cb}}, J_{21}) = \frac{M_{\text{mol,crit}}}{(1+z)^{3/2}} f_{v_{\text{cb}}}(v_{\text{cb}}) f_{\text{LW}}(J_{21}), \quad (5)$$

where  $M_{\text{mol,crit}} = 3.3 \times 10^7 M_{\odot}$  is the (no feedback) molecular cooling threshold, corresponding to  $T_{\text{vir}} \approx 10^3 \text{ K}$  (e.g. Barkana & Loeb 2001), and  $f_{\text{LW}}$  and  $f_{v_{\text{cb}}}$  are the strength of Lyman–Werner and relative-velocity feedback, respectively.

The strength of the Lyman–Werner feedback is parametrized as (Machacek, Bryan & Abel 2001; Visbal et al. 2014):

$$f_{\text{LW}}(J_{21}) = 1 + A_{\text{LW}} \times (J_{21})^{\beta_{\text{LW}}}, \quad (6)$$

where  $A_{\text{LW}}$  and  $\beta_{\text{LW}}$  are free parameters. In the following, we set  $\beta_{\text{LW}} = 0.6$ , as simulations predict a small range for this parameter (e.g. Skinner & Wise 2020; Kulkarni, Visbal & Bryan 2021; Schauer et al. 2021) and leave  $A_{\text{LW}}$  free, and study whether it can be determined from observations. We model the LW intensity,  $J_{21}$ , in the same way as Qin et al. (2020), using the PopII- and PopIII-dominated spectral energy distributions (SEDs) from Barkana & Loeb (2005) to calculate the LW emissivity.

The strength of the relative-velocity feedback is modelled as

$$f_{v_{\text{cb}}}(v_{\text{cb}}) = \left(1 + A_{v_{\text{cb}}} \frac{v_{\text{cb}}}{\sigma_{\text{cb}}}\right)^{\beta_{v_{\text{cb}}}}, \quad (7)$$

where  $\sigma_{\text{cb}} \approx 30 \text{ km s}^{-1}$  is the rms velocity (Tselikhovich & Hirata 2010). We follow Muñoz et al. (2022) and use  $A_{v_{\text{cb}}} = 1$  and  $\beta_{v_{\text{cb}}} = 1.8$ , as these values have been recovered consistently in independent simulations (Kulkarni et al. 2021; Schauer et al. 2021).

The stellar mass ( $M_{\star}$ ) to halo mass ratio is described by a power law (e.g. Moster, Naab & White 2013; Behroozi & Silk 2015; Mutch et al. 2016; Sun & Furlanetto 2016; Tacchella et al. 2018; Yung et al. 2020; Sabti, Muñoz & Blas 2022a, b)

$$\frac{M_{\star}}{M_{\text{h}}} = \frac{\Omega_b}{\Omega_m} \times \min \left[ 1, \begin{cases} f_{\star,10}^{\text{II}} \left(\frac{M_{\text{h}}}{10^{10} M_{\odot}}\right)^{\alpha_{\star}^{\text{II}}} & \text{PopII} \\ f_{\star,7}^{\text{III}} \left(\frac{M_{\text{h}}}{10^7 M_{\odot}}\right)^{\alpha_{\star}^{\text{III}}} & \text{PopIII} \end{cases} \right], \quad (8)$$

with four free parameters ( $f_{\star,10}^{\text{II}}$ ,  $\alpha_{\star}^{\text{II}}$ ,  $f_{\star,7}^{\text{III}}$ ,  $\alpha_{\star}^{\text{III}}$ ) which set the normalization at the pivot mass and low mass slope for galaxies forming population II and population III stars, respectively. We note that although the stellar mass – halo mass relation turns over at high masses ( $M_{\text{h}} \sim 10^{12} M_{\odot}$ ; e.g. Behroozi et al. 2013; Mason, Trenti & Treu 2015), the radiation fields at these high redshifts are determined by the vast majority of haloes which have much lower masses; thus a single power-law slope suffices for our purposes. This power-law slope encapsulates additional mass-dependent feedback processes, such as supernovae feedback.

We assume the star-formation rate in haloes is related to their dynamical time, which during matter domination scales as  $H^{-1}$ , to give us

$$\frac{dM_{\star}}{dt} = \frac{M_{\star}}{t_{\star} H(z)^{-1}}, \quad (9)$$

where  $t_{\star}$  can be a free parameter, but as SFR has the ratio  $f_{\star}/t_{\star}$  there is a strong degeneracy between these parameters (Park et al. 2019), and  $t_{\star}$  can typically be set to a constant.

<sup>6</sup>Halo mass functions are created using the Extended Press-Schechter formalism (e.g. Sheth, Mo & Tormen 2001) using a top-hat window function.

**Table 1.** 21CMFAST parameters and their fiducial values for our two runs. For a detailed description, see Section 2.1.

Parameter	Description	Population	Park et al. (2019)		EOS21 (Muñoz et al. 2022)	
			Fiducial	Vary?	Fiducial	Vary?
$\alpha_{\star}^{\text{II}}$	Stellar–halo mass power-law slope	II	0.50	✓	0.50	✓
$\log_{10} f_{\star,10}^{\text{II}}$	Stellar–halo mass normalization (at $M_h = 10^{10} M_{\odot}$ )	II	−1.30	✓	−1.25	✓
$t_{\star}$	SFR timescale as a fraction of the Hubble time	both	0.50	✓	0.50	–
$\log_{10} M_{\text{turn}}$	Halo mass turnover for atomic cooling haloes [ $M_{\odot}$ ]	II	8.7	✓	–	–
$\alpha_{\star}^{\text{III}}$	Stellar–halo mass power-law slope	III	–	–	0.0	✓
$f_{\star,7}^{\text{III}}$	Stellar–halo mass normalization (at $M_h = 10^7 M_{\odot}$ )	III	–	–	−2.50	✓
$\alpha_{\text{esc}}$	Ionizing escape fraction–halo mass power-law slope	both	−0.50	✓	−0.30	✓
$\log_{10} f_{\text{esc},10}^{\text{II}}$	Ionizing escape fraction normalization (at $M_h = 10^{10} M_{\odot}$ )	II	−1.00	✓	−1.35	✓
$\log_{10} f_{\text{esc},7}^{\text{III}}$	Ionizing escape fraction normalization (at $M_h = 10^7 M_{\odot}$ )	III	–	–	−1.35	✓
$\log_{10} L_X^{\text{II}}/\dot{M}_{\star}$	X-ray luminosity per SFR [ $\text{erg s}^{-1} M_{\odot}^{-1} \text{yr}$ ]	II	40.5	✓	40.5	✓
$\log_{10} L_X^{\text{III}}/\dot{M}_{\star}$	X-ray luminosity per SFR [ $\text{erg s}^{-1} M_{\odot}^{-1} \text{yr}$ ]	III	–	–	40.5	$= \log_{10} L_X^{\text{II}}$
$E_0$	minimum X-ray energy which escapes galaxies [eV]	both	500	✓	500	✓
$A_{\text{vcb}}$	Amplitude of DM–baryon relative velocity feedback	III	–	–	1.00	–
$A_{\text{LW}}$	Amplitude of Lyman–Werner feedback	III	–	–	2.00	✓

Galaxies hosting population II and population III stars can also have different hydrogen ionizing photon escape fractions

$$f_{\text{esc}} = \begin{cases} f_{\text{esc},10}^{\text{II}} \left( \frac{M_h}{10^{10} M_{\odot}} \right)^{\alpha_{\text{esc}}} & \text{Pop II} \\ f_{\text{esc},7}^{\text{III}} \left( \frac{M_h}{10^7 M_{\odot}} \right)^{\alpha_{\text{esc}}} & \text{Pop III,} \end{cases} \quad (10)$$

where  $f_{\text{esc},10}^{\text{II}}$  and  $f_{\text{esc},7}^{\text{III}}$  set the normalization of the escape fractions and  $\alpha_{\text{esc}}$  their power-law slopes. Note that, for simplicity, we take  $\alpha_{\text{esc}}$  to be the same for each population of galaxies as we assume it is a function of halo mass only.

These early populations of galaxies are also expected to produce X-rays, most likely from high mass X-ray binaries (e.g. Furlanetto 2006; Mineo, Gilfanov & Sunyaev 2011; McQuinn 2012; Fragos et al. 2013). We assume the specific X-ray luminosity is proportional to the galaxy SFR and the X-ray SED is a power law with energy spectral index = −1, such that the specific X-ray luminosity per unit SFR is

$$\frac{dL_X/\dot{M}_{\star}}{dE} = \frac{E^{-1}}{\int_{E_0}^{2 \text{ keV}} dE E^{-1}} \times \begin{cases} L_{X,<2\text{keV}}^{\text{II}}/\dot{M}_{\star} & \text{Pop II} \\ L_{X,<2\text{keV}}^{\text{III}}/\dot{M}_{\star} & \text{Pop III,} \end{cases} \quad (11)$$

where  $L_{X,<2\text{keV}}^{\text{II}}/\dot{M}_{\star}$  and  $L_{X,<2\text{keV}}^{\text{III}}/\dot{M}_{\star}$  are the total soft-band X-ray luminosity per unit SFR in atomic cooling and molecular cooling galaxies, respectively. In the following, we refer to these as  $L_X^{\text{II}}/\dot{M}_{\star}$  and  $L_X^{\text{III}}/\dot{M}_{\star}$  and assume they have the same value =  $L_X/\dot{M}_{\star}$ , motivated by simulations of high mass X-ray binaries in metal-poor environments in the early universe (Fragos et al. 2013) – though it is possible to vary them independently.  $E_0$  is the cutoff in X-ray energies which can escape galaxies (e.g. X-rays with energy  $< E_0$  are absorbed by the ISM of the host galaxies and thus do not interact with the IGM (e.g. Das et al. 2017). X-rays at higher energies ( $E > 2 \text{ keV}$ ) have a mean free path greater than the Hubble length and thus also do not efficiently heat the IGM.

The astrophysical model described above has a total of 14 free parameters. A summary of these parameters and which ones we vary in our analyses is given in Table 1.

## 2.2 Modelling the 21-cm signal

Hydrogen atoms have heavily disallowed hyperfine transitions, key amongst them is the 21-cm line between the singlet and triplet states

of the  $^1\text{S}$  orbital. The rate of these ‘spin-flip’ transitions is determined by the relative population of atoms in either states

$$\frac{n_1}{n_0} = \frac{g_1}{g_0} e^{-\frac{T_{\star}}{T_S}} \quad (12)$$

where  $g_i$  are the spin degeneracy factors of each state (with  $g_1/g_0 = 3$  for 21-cm transitions),  $T_{\star} = E_{10}/k_B = 68 \text{ mK}$  corresponding to the transition energy  $E_{10}$ , and  $T_S \gg T_{\star}$  is the *spin temperature*. In the early universe,  $T_S$  is coupled to the kinetic temperature of the IGM through collisional excitations (Loeb & Zaldarriaga 2004), but by  $z \sim 30$  collisions become rarer and interactions with CMB photons dominate, driving a thermal equilibrium between  $T_S$  and  $T_{\text{CMB}}$ , resulting in no net absorption or emission of 21-cm photons relative to the CMB blackbody. However, once the first stars form ( $z \sim 20$ – $30$ ), this thermal equilibrium is broken due to the injection of Ly  $\alpha$  photons (the Wouthuysen–Field effect; e.g. Hirata 2006) and the spin temperature couples to the lower temperature of the IGM gas, resulting in a net absorption of CMB photons at 21-cm wavelengths. Later, as the IGM is heated by X-rays from the first galaxies ( $z \sim 10$ – $15$ ), the spin temperature exceeds the CMB temperature resulting in a net emission of 21-cm photons. Once hydrogen is reionized ( $z \sim 6$ – $10$ ), the density of neutral hydrogen drops dramatically and the cosmological 21-cm signal is negligible (see e.g. Furlanetto, Oh & Briggs 2006; Morales & Wyithe 2010; Pritchard & Loeb 2012, for reviews).

The goal of Cosmic Dawn 21-cm experiments is to measure the 21-cm brightness temperature,  $T_{21}$ , the offset of the 21-cm signal relative to the temperature of the cosmic microwave background,  $T_{\text{CMB}}$  (e.g. Furlanetto et al. 2006):

$$T_{21} = \frac{T_S - T_{\text{CMB}}}{1 + z} (1 - e^{-\tau_{21}}) \quad (13)$$

$$\approx 27 x_{\text{HI}} (1 + \delta) \frac{H(z)}{dv_r/dr + H(z)} \left( 1 - \frac{T_{\text{CMB}}}{T_S} \right) \times \left( \frac{1 + z}{10} \frac{0.15}{\Omega_m h^2} \right)^{1/2} \left( \frac{\Omega_b h^2}{0.023} \right) \text{ mK.} \quad (14)$$

where the second line is the  $\tau_{21} \ll 1$  Taylor expansion. Here,  $x_{\text{HI}}$  is the neutral hydrogen fraction,  $T_S$  is the spin temperature of the gas,  $\delta = \rho/\bar{\rho} - 1$  is the overdensity of the gas, and  $dv_r/dr$  is the gradient of the line-of-sight velocity component. All quantities are computed at  $z = \nu_0/\nu - 1$ , where  $\nu_0 = 1420 \text{ MHz}$  is the 21-cm rest-frame

frequency. This Taylor expansion is useful for physical intuition, though we note that 21CMFAST computes the full  $\exp(-\tau_{21})$  term.

To create the neutral fraction, spin temperature, density, and velocity fields required to find  $T_{21}$ , we use the public code 21CMFAST (Mesinger et al. 2011; Park et al. 2019; Murray et al. 2020), using the astrophysical model described above in Section 2.1 and we refer the reader to these works and references therein. In Section 2.4, we describe the parameters and setup for our 21CMFAST simulations.

### 2.3 Fisher-matrix formalism

Given a posterior distribution  $P(\theta|\text{data})$  for model parameters  $\theta$ , the Fisher-matrix components are given by

$$\mathcal{F}_{ij} = - \left\langle \frac{\partial^2 \ln P}{\partial \theta_i \partial \theta_j} \right\rangle, \quad (15)$$

The Cramér–Rao theorem states that any unbiased estimator for the parameters will produce a covariance matrix that is no more accurate than  $\mathcal{F}^{-1}$ : thus the Fisher matrix can be used to estimate the minimum uncertainties of parameters given observations (e.g. Albrecht et al. 2009).

Here, we focus on the 21-cm power spectrum but the same analysis can be done with the 21-cm global signal (e.g. Liu et al. 2013; Muñoz et al. 2020), or any other observable. Previous works have used Fisher-matrix analyses of simulated 21-cm observations with 21cmfast to forecast constraints, for example, on reionization and cosmological parameters, and small-scale dark-matter structure (e.g. Pober et al. 2014; Ewall-Wice et al. 2016; Liu & Parsons 2016; Shimabukuro et al. 2017; Muñoz et al. 2020; Shaw, Bharadwaj & Mondal 2020; Greig, Ting & Kaurov 2022). However, these works all used a restricted parameter space, with most using the 3 parameter astrophysical model of 21CMFAST v1. Here, we will use the extended 21CMFAST v3 parameter space (with 14 total degrees of freedom), which characterizes the UV and X-ray emission from both population II and III star formation, as detailed in Section 2.1.

Given a list of parameters  $\theta_i$ , and assuming the posterior distribution can be described as Gaussian (i.e.  $\ln P \propto -\chi^2$ ), we define the Fisher matrix for the 21-cm power spectrum  $\Delta_{21}^2(k, z)$  as

$$\mathcal{F}_{ij} = \frac{\partial^2 \chi^2}{\partial \theta_i \partial \theta_j} = \sum_{i_k, i_z} \frac{\partial \Delta_{21}^2(k, z)}{\partial \theta_i} \frac{\partial \Delta_{21}^2(k, z)}{\partial \theta_j} \frac{1}{\sigma_{\Delta_2}^2(k, z)}, \quad (16)$$

where  $\sigma_{\Delta_2}^2$  is the measurement error in the power spectrum with  $k$  bin  $i_k$  and  $z$  bin  $i_z$ , and we have assumed uncorrelated errors between  $k$  and  $z$  bins (in principle, we can compute the full measurement covariance matrix but we follow the assumption of uncorrelated errors to more easily compare to previously published MCMC results, e.g. Park et al. 2019). Our code 21CMFISH calculates the derivatives with respect to a set of input parameters to produce the Fisher matrix (equation 16).

The inverse of the Fisher matrix is the covariance matrix  $\mathcal{C} = \mathcal{F}^{-1}$ , and with this definition, it is easy to see that the forecasted uncertainty in the  $i$ th parameter is simply  $\sigma(\theta_i) = \sqrt{\mathcal{C}_{ii}}$ .

### 2.4 Simulated 21-cm observations and uncertainties

As described in Section 2.3 above, we can use the Fisher matrix to derive the lowest possible estimate of the parameter uncertainties given observations. In this work, we generate parameter constraints from two sets of mock observations, each serving a specific purpose

(i) We validate our Fisher-matrix approach by comparing to the MCMC posterior of Park et al. (2019). We use their fiducial parameters, which only includes population II star formation in atomic-cooling galaxies. Simulation boxes have a comoving volume of  $(250 \text{ Mpc})^3$  on a  $128^3$  grid from  $z = 5.9$ –28 following Park et al. (2019) to match the HERA observing bandwidth.

(ii) An exploration of the updated ‘Evolution of Structure’ (EOS21) simulation presented by Muñoz et al. (2022)<sup>7</sup>. The EOS21 parameters include star formation in minihaloes, and the impact of Lyman–Werner feedback and relative velocities between baryons and dark matter. The PopII parameters are based on those inferred by Qin et al. (2021b), who used the Planck Collaboration XLVII (2016) electron scattering optical depth, rest-frame UV luminosity functions (LFs; Bouwens et al. 2015), dark pixel fraction (McGreer, Mesinger & D’Odorico 2015), and Ly $\alpha$  forest optical depth (Bosman et al. 2018) in their likelihood. On the other hand, the PopIII parameters are difficult to constrain with current observations, and so were chosen fairly arbitrarily. We note that PopIII star formation in their fiducial model only dominates the total SFRD at  $z \gtrsim 15$ . The simulation boxes we use have a comoving volume of  $(400 \text{ Mpc})^3$  on a  $200^3$  grid from  $z = 5$ –30.

The fiducial parameters for these runs are given in Table 1. Our motivation for choosing these sets of fiducial parameters is that they produce UV LFs, a reionization history and CMB scattering optical depth that are consistent with current observations at  $z \sim 6$ –10, and so are thus likely to represent a reasonable parameter space for high redshift galaxy properties. We use  $\geq (250 \text{ Mpc})^3$  to ensure convergence of the power spectrum in the range  $\sim 0.1$ –1  $\text{Mpc}^{-1}$  which we will consider below, following Kaur, Gillet & Mesinger (2020). Our resolution of  $\approx 2 \text{ Mpc}$  per voxel should also provide a converged power spectrum: Greig et al. (2022) demonstrated that this resolution, with a similar volume to our simulations, provides converged wavelet scattering transformation coefficients (a non-Gaussian probe, complementary to the power spectrum) for the 21-cm signal.

21-cm power spectra are generated by dividing light-cones into ‘chunks’ following Greig & Mesinger (2018). For our comparisons with Park et al. (2019), we follow their approach and divide the light-cones into 12 chunks of equal comoving volume. For our EOS21 run, we divide the light-cone into chunks corresponding to 8 MHz bandwidths, which more closely resembles what would be done with data. The 21-cm global signal, reionization history and power spectra at a few redshifts for the two models are plotted in Fig. 1.

To calculate the Fisher matrices, we vary each parameter  $\pm 3$  per cent of its fiducial value and calculate two-sided derivatives<sup>8</sup>, finding the variation step-size such that the derivatives were converged. We tested convergence of the derivatives and found  $\pm 3$  per cent worked in all cases with the exception of  $\log_{10} L_X/\dot{M}_*$  which we varied by  $\pm 0.1$  per cent and  $\log_{10} M_{\text{turn}}$  which we vary by  $\pm 1$  per cent, as these parameters have narrower likelihoods in the 21-cm signal. We verified that one-sided derivatives produced almost identical values.

Thus, to create a derivative  $\partial \Delta_{21}^2(k, z)/\partial \theta_i$  for each parameter, we use 3 simulated power spectra: the fiducial, one setting the parameter to  $\theta_i(1 + X)$  and one with  $\theta_i(1 - X)$ , where  $X$  is the variation (usually

<sup>7</sup>Simulation data available at: [https://www.dropbox.com/sh/dqh9r6wb0s68jfo/AACc9ZCqsN0SQ\\_JJN7GRVuqDa?dl=0](https://www.dropbox.com/sh/dqh9r6wb0s68jfo/AACc9ZCqsN0SQ_JJN7GRVuqDa?dl=0)

<sup>8</sup>The variation is in either linear or logarithmic quantities corresponding to the parameters in Table 1, i.e. we vary  $\log_{10} f_{\star,10}^H \pm 3$  per cent of its fiducial value.

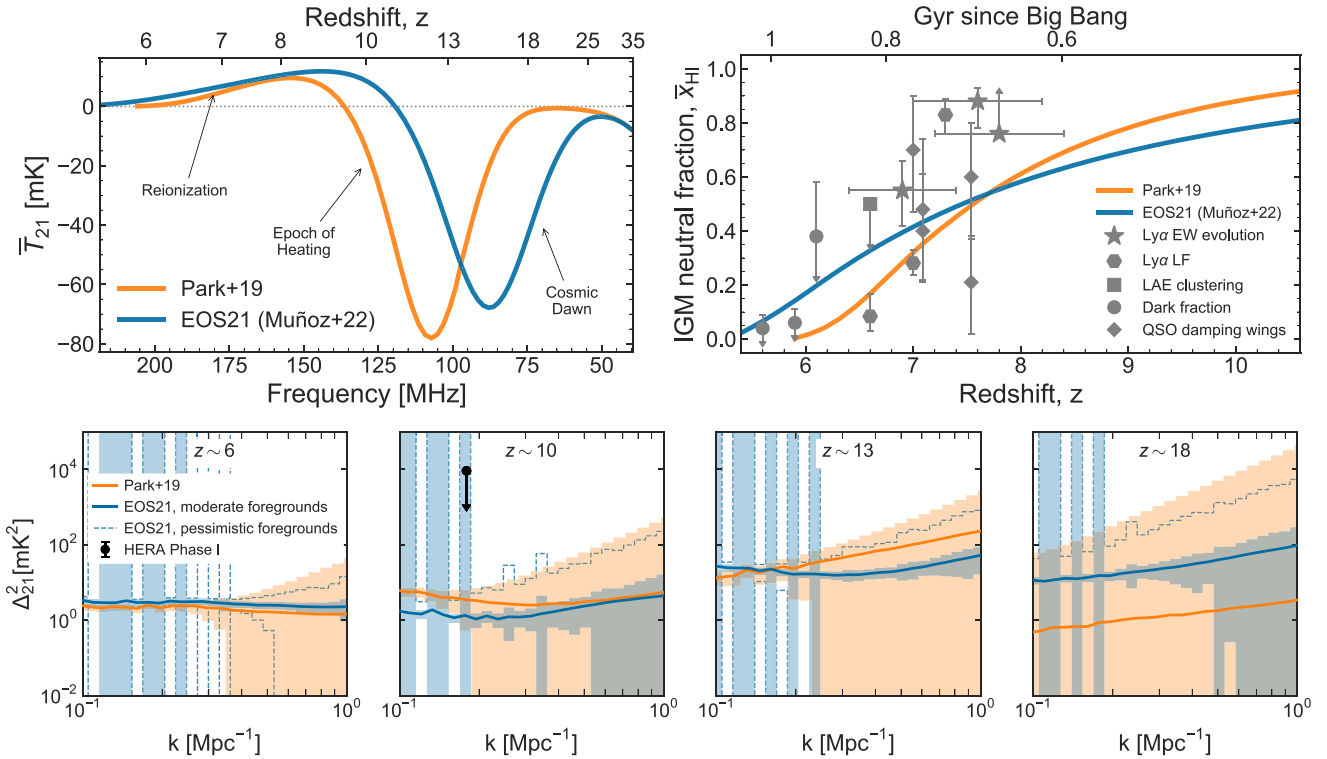


**Figure 1.** Comparison of our two fiducial models, with Park et al. (2019) in orange, EOS21 in blue. **Top left:** Global 21-cm signal. **Top right:** reionization history. We also plot reionization history constraints derived from observations of the Ly $\alpha$  equivalent width distribution (star, Mason et al. 2018; Hoag et al. 2019; Mason et al. 2019; Whittler et al. 2020); the Ly $\alpha$  luminosity function (hexagon; Morales et al. 2021), the clustering of Ly $\alpha$  emitting galaxies (square; Ouchi et al. 2010; Sobacchi & Mesinger 2015); Ly $\alpha$  and Ly $\beta$  forest dark pixel fraction (circle; McGreer et al. 2015); and QSO damping wings (diamond, Greig et al. 2017; Davies, Becker & Furlanetto 2018; Greig, Mesinger & Bañados 2019; Wang et al. 2020). **Lower:** example power spectra of our two fiducial models at four redshifts. We show our fiducial ‘moderate’ HERA noise estimates for each case as the filled regions, and the ‘pessimistic’ noise as dashed blue line, including Poisson noise and a 20 per cent modelling error added in quadrature. We show the errors only in the  $k$ -space window, where we calculate the likelihood (0.1–1 Mpc $^{-1}$ ). Note that, due to a spline interpolation of the power spectra errors by Park et al. (2019), the low  $k$  noise estimates are smooth, unlike those in the EOS21 model. For comparison, we also plot the 95 per cent confidence upper limit at  $z = 10.4$  from HERA Phase I observations (The HERA Collaboration et al. 2022b).

3 per cent as described). As we only need to create one fiducial simulation, for  $N$  parameters, we create a total of  $2N + 1$  simulations to calculate the Fisher matrix (equation 16).

To make forecasts for upcoming observations with HERA, we use the PYTHON package 21CMSENSE<sup>9</sup> (Pofer et al. 2014). We run three different setups, which we now describe. For the comparison with Park et al. (2019), we use the same noise as their study, which is essentially identical to the ‘pessimistic’ case described below. The noise was calculated assuming 1000 h of observation using 331 antennae.

For our EOS21 forecasts (with PopIII stars in molecular cooling galaxies), we find the noise in two cases, with moderate and pessimistic foregrounds, respectively. The dominant sources of noise for 21-cm observations are the instrumental noise of the antennae and large foreground contamination, from both our Galaxy and the atmosphere. The combination of these noise sources can be parametrized by a ‘system temperature’,  $T_{\text{sys}}(\nu)$  which is the total observed 21-cm brightness temperature (e.g. Morales & Wyithe 2010). The foregrounds substantially contaminate the signal in the Fourier plane, particularly in the so-called ‘wedge’ (e.g. Liu et al. 2009; Pofer et al. 2013; Liu & Shaw 2020), within wavenumbers  $k_{\parallel}$

$\leq a + bk_{\perp}$ . Here,  $k_{\parallel}$  and  $k_{\perp}$  are the wavenumbers in the line-of-sight and perpendicular direction, and  $a$  (called the super-horizon buffer in 21CMSENSE) and  $b$  are constants that parametrize the severity of the foregrounds and thus which regions of  $k$ -space will be discarded in the analysis.

In the moderate foregrounds case, we use the ‘moderate’ foregrounds model in 21CMSENSE, with a wedge superhorizon buffer  $a = 0.1 h \text{ Mpc}^{-1}$  and a HERA system temperature (DeBoer et al. 2017) of

$$T_{\text{sys}}(\nu) = 100 \text{ K} + 120 \text{ K} (\nu/150\text{MHz})^{-2.55}. \quad (17)$$

In the pessimistic case, we increase the wedge horizon buffer to  $a = 0.15 h \text{ Mpc}^{-1}$ , and use the default system temperature in 21CMSENSE, which is  $\sim 3 \times$  larger than that of equation (17) (Pofer et al. 2014). In both cases, the antennae temperature is the same but this larger system temperature is motivated by the sky temperature measured by LOFAR (van Haarlem et al. 2013). In the pessimistic case, the signal-to-noise ratio of the power spectrum is lower by nearly an order of magnitude, and consequently increases the error bars on each parameter by approximately a factor of three, as we will see Figs 3 and 5. This pessimistic case is comparable to that used in the forecasts by Park et al. (2019). In both moderate and pessimistic cases for EOS21, we assume 1 yr (1080 h) of data using 331 antennae

<sup>9</sup><https://github.com/jpofer/21cmSense>

across the 50–250 MHz range (corresponding to the redshifts  $z \sim 5$ –28), divided in equal-width bands of 8 MHz.

In all cases, we follow Park et al. (2019) and add Poisson noise (from the finite-size simulations) and a 20 per cent modelling error to the power spectra in quadrature in addition to the Poisson noise for the mock observations. We calculate the likelihood only in the  $k$ -space window  $0.1$ – $1 \text{ Mpc}^{-1}$ , corresponding roughly to limits on the foreground noise and the shot noise, respectively. For the Park et al. (2019) comparison, we calculate the likelihood over the redshift range  $z = 5.9$ – $28.0$  to match their analysis, and for EOS21, we calculate the likelihood over  $z = 5.0$ – $28.0$ .

### 3 RESULTS

Section 3.1 describes the validation of our Fisher-matrix approach by comparison to an MCMC by Park et al. (2019). Section 3.2 presents forecasted constraints on the population II and population III galaxy formation parameter space expected with HERA 1 yr observations, assuming the EOS21 model from Muñoz et al. (2022). Section 3.3 presents the principal components of the Fisher matrix, providing insight into the best constrained linear combinations of parameters. In Section 3.4, we evaluate whether the Fisher matrix can be used for inference.

#### 3.1 Comparison with Park et al. (2019) population II-only MCMC

To verify our Fisher-matrix approach, we compare with the MCMC analysis by Park et al. (2019). Park et al. (2019) carried out an inference on mock HERA observations to infer properties of population II galaxies. The parameters varied in this analysis are listed in Table 1.

To compare with Park et al. (2019), we construct simulations using the same dimensions and redshift range, as described in Section 2.2, and with the same fiducial parameters, though with different initial conditions. We then divide light-cones into 12 chunks of equal comoving volume to create power spectra, replicating their approach, and calculate the derivatives of the power spectrum with respect to the parameters of interest as described in Section 2.3. To create the Fisher matrix (equation 16) we use the same HERA noise estimate  $\sigma[\Delta^2(k, z)]$  as Park et al. (2019), which was obtained using 21CMSENSE. To obtain the total uncertainty on the power spectrum, we add in quadrature the HERA thermal noise plus the cosmic variance plus a 20 per cent ‘modelling uncertainty’ on the power spectrum, again following Park et al. (2019).

The resulting  $1, 2\sigma$  error ellipses obtained using our Fisher matrix are shown in Fig. 2, along with the 21cm-only<sup>10</sup> MCMC posteriors by Park et al. (2019). We note that we plot the MCMC chains produced by Park et al. (2019), but do not exactly reproduce their published posteriors and 68 per cent credible intervals due to some small differences in burn-in steps and removal of local minima in the posterior between that work and ours. The chains have 229 steps and 35 walkers. We remove the first 50 per cent of steps as burn-in and also remove  $\sim 24$  per cent of the chains which we identify as falling into local minima. The median maximum likelihood for the MCMC was  $\mathcal{L}_{\text{max}} \sim 10^{-4}$  and we remove chains in local minima –where the likelihood in the final step is  $< 10^{-10}$ .

<sup>10</sup>Park et al. (2019) also show posteriors obtained by combining existing UV LF observations with the mock 21 cm power spectra in the likelihood.

Our Fisher-matrix approach clearly recovers the inferred degeneracies between parameters in all cases, and produces comparable uncertainties to those estimated using the MCMC. The MCMC contours and the Fisher ellipses are oriented similarly and have similar ellipticities demonstrating that the correlations between parameters are well captured by the Fisher matrix analysis. The marginalized 68 per cent credible intervals on each parameter obtained with the Fisher matrix are within 40 per cent of those obtained with the MCMC (with the exception of  $E_0$  where the Fisher error is  $\sim 50$  per cent of the MCMC value). These results do not change significantly if we use the median inferred parameters obtained by Park et al. (2019), implying any difference in uncertainties is dominated by the approximation of the posterior as Gaussian, rather than the position of the posterior peak. As noted in Section 2.3, the Fisher matrix will give the minimum uncertainties, so we do expect our technique to slightly underestimate the errors compared to a full mapping of the posterior. Nevertheless, this remarkable agreement validates our Fisher matrix approach as an efficient tool to explore 21-cm observational constraints on cosmology and astrophysics, providing the parameter degeneracies remain approximately Gaussian, dramatically reducing the need for expensive MCMC runs. For comparison, the MCMC run by Park et al. (2019) required 70 000 individual simulations, whereas our Fisher-matrix approach required only 17.

The parameter where the Fisher-matrix constraints are most different from the MCMC is  $\alpha_*^{\text{II}}$ . This is because Park et al. (2019) set a uniform prior on  $\alpha_*^{\text{II}} = [-0.5, 1]$ , whereas in the Fisher-matrix approach, we do not set any bounding conditions and make the assumption of a Gaussian likelihood, so the confidence ellipse can extend to  $\alpha_*^{\text{II}} > 1$ , making it broader than the MCMC posterior.

Due to using the ‘pessimistic’ foreground model assumed (see Section 2.4), these forecasts find most parameters will be measured at the 20–30 per cent error level, with the exception of X-ray parameters and  $M_{\text{turn}}$  which can be measured to  $< 10$  per cent precision, whereas  $\alpha_*^{\text{II}}$  and  $\alpha_{\text{esc}}$  are more difficult to measure precisely. As discussed by Park et al. (2019), the inclusion of independent observations that can constrain galaxy formation properties, for example the UV luminosity function, can break degeneracies and reduce parameter uncertainties to  $\lesssim 10$  per cent precision.

#### 3.2 Extended parameter space forecast

Given that our Fisher-matrix approach recovers the same degeneracies and very similar confidence intervals as an MCMC, we now make a forecast in an unexplored regime: 10 free astrophysical parameters governing both population II and population III galaxy formation, and the impact of streaming velocities and Lyman–Werner feedback on the formation of minihaloes, over the full redshift range of the Cosmic Dawn 21-cm signal ( $z \sim 5$ –30). Due to computational expense and current instrumental sensitivity, previous works have performed MCMC or Nested sampling in a more limited parameter space, varying only PopII or PopIII parameters at a time (e.g. Qin et al. 2021a; The HERA Collaboration et al. 2022a, explored 7 and 9 parameters, respectively, roughly requiring  $\sim 10^5$  individual simulations and  $\sim 100 \text{ k CPUh}$ ). Our 21CMFISH calculation, by contrast, required only 21 individual simulations (as we fixed  $L_X^{\text{II}}/M_* = L_X^{\text{III}}/M_*$ ). Although the Fisher matrix assumes a multivariate Gaussian posterior and the setting of physical priors is less straightforward, these are reasonable approximations when the posterior is unimodal and narrowly peaked around the maximum likelihood value (e.g. Trotta 2008). Indeed, we expect future HERA and SKA observations to be highly constraining, making Fisher

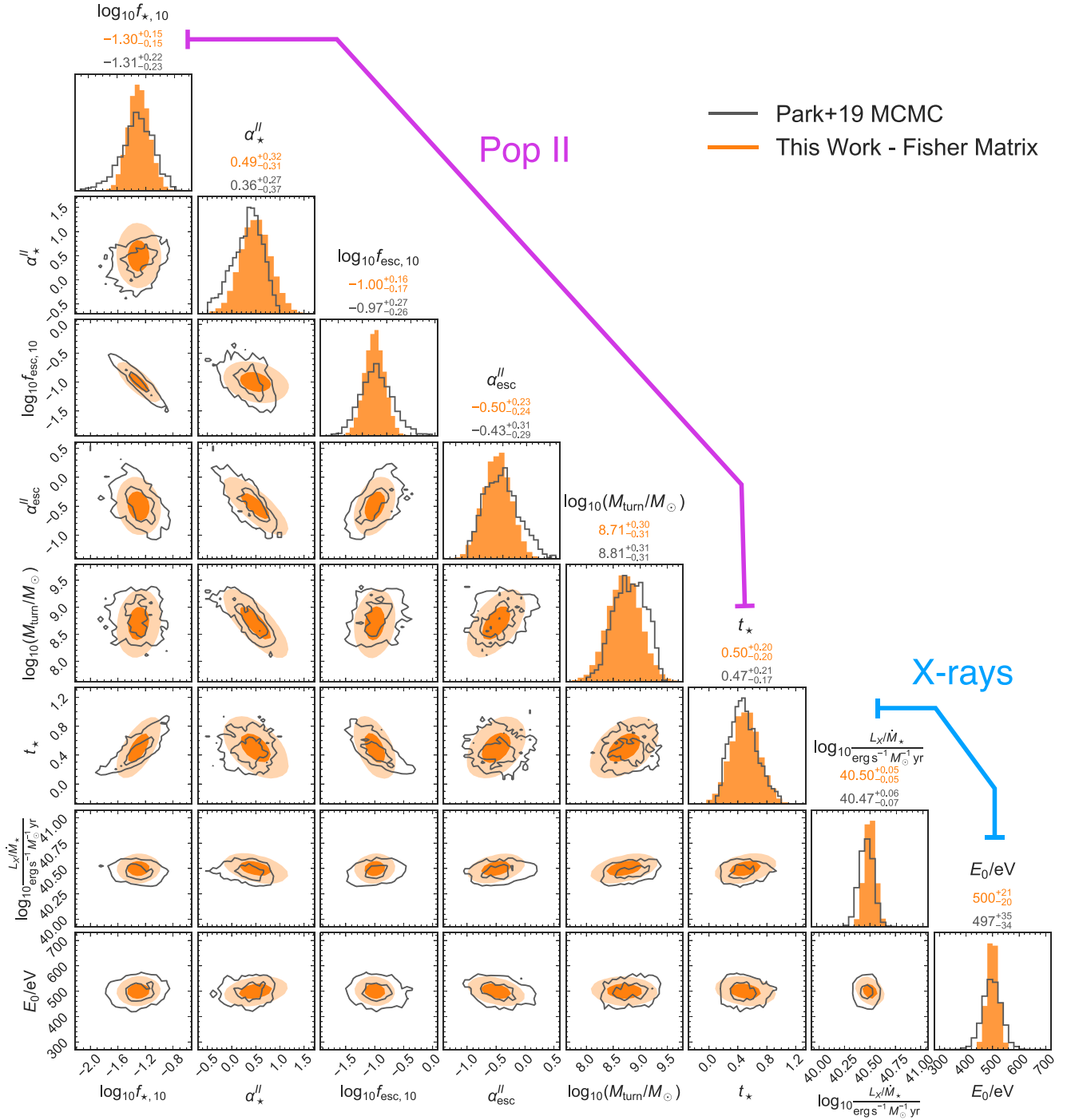


**Figure 2.** Validation of our Fisher-matrix technique by comparison with the MCMC runs of Park et al. (2019). We plot parameter constraints from Park et al. (2019) (grey line) and our results (orange filled). The top right plots show 1D marginalized posteriors and the lower triangle plots show the 2D marginalized posteriors. The contours show 1, 2 $\sigma$  confidence intervals for the posteriors. Our Fisher-matrix approach recovers the same degeneracies as the MCMC and comparable uncertainties, while requiring  $\sim 10^4$  fewer simulations.

forecasts useful approximations of the true posterior for futuristic data sets.

Fig. 3 shows the forecasted parameter constraints from our Fisher-matrix approach for 10 EOS21 fiducial free parameters (Muñoz et al. 2022). The contours show 1, 2 $\sigma$  confidence intervals for the parameters. For this forecast, we assume one year (i.e. 1080 h) of HERA data, and show the forecasts for mod-

erate and pessimistic foreground noise levels, as described in Section 2.4.

The fractional error estimated for each parameter is plotted in Fig. 4. With moderate foreground noise it would be possible to infer nearly all parameters to  $\lesssim 10$ –30 per cent precision, with the exception of the amplitude of Lyman–Werner feedback,  $A_{LW}$ , which is much more poorly constrained—due to its smaller impact on the amplitude of the

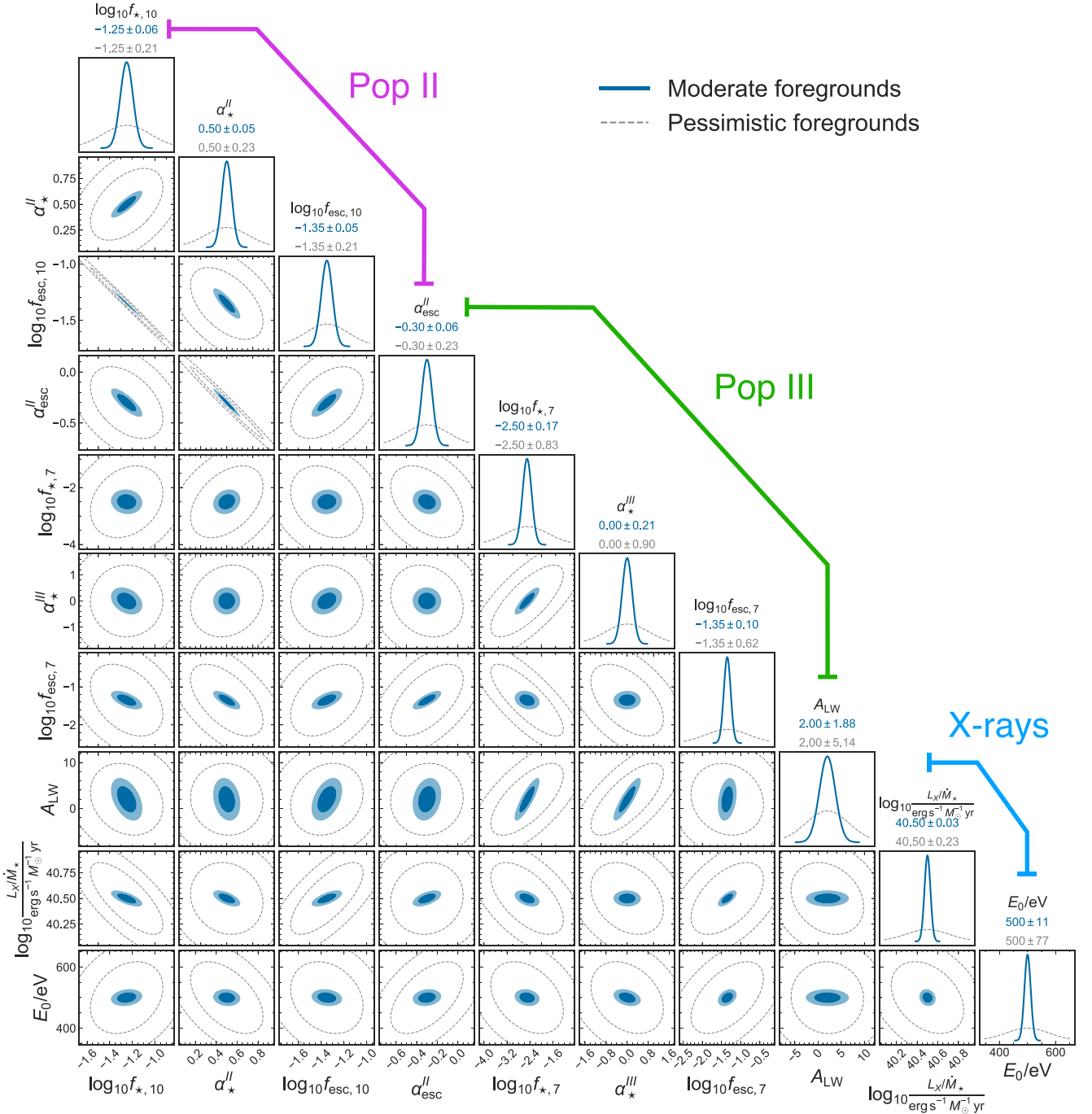


**Figure 3.** Parameter constraints for the fiducial EOS21 run, using the parameters defined by Muñoz et al. (2022) for moderate (blue solid) and pessimistic (grey dashed) foregrounds in HERA 1-yr observations, as described in Section 2.4. The contours show 1 and  $2\sigma$  confidence intervals and the quoted confidence interval for the 1D constraint is  $1\sigma$ .

21-cm signal (Muñoz et al. 2022), and X-ray parameters which can be constrained to  $< 10$  per cent. This demonstrates 21-cm observations will be a powerful tool to learn about the formation of the first galaxies. As expected, parameter constraints would be substantially worse in the case of ‘pessimistic’ foreground noise, particularly on population III parameters. This is because the foreground noise is a strong function of frequency and thus redshift, with the lowest noise in the  $z < 10$  – Epoch of Reionization – window, which is dominated by population II-hosting galaxies. This can be seen clearly

in the signal-to-noise ratio of our fiducial 21-cm power spectrum as a function of redshift for the two noise models, which we plot in Fig. 5.

We find that most parameters for *both* population II and III galaxies could be measured at  $< 10$  per cent precision under the assumption of moderate instrumental noise. This is due to the relative redshift dependence of the parameters and the wide frequency/redshift range of the HERA observations. In Fig. 6, we plot the redshift dependence of the fractional error on each parameter, calculated in rolling

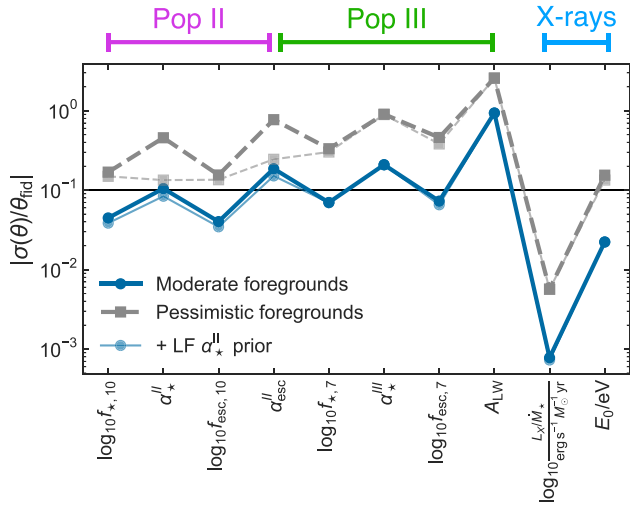


**Figure 4.** Fractional  $1\sigma$  error in each parameter as estimated from the Fisher matrix, for the moderate (blue solid line) and pessimistic (grey dashed line) foreground noise models (see Section 2.4). In both cases, the thick lines show the HERA-only constraints and the thin solid lines in the same colour and style show the fractional error estimate after including a prior on  $\alpha_*^{\text{II}}$  from the UV LF using Hubble data. The  $\alpha_*^{\text{II}}$  prior reduces the uncertainty on population II parameters by approximately a factor of three. We mark the 10 per cent fractional uncertainty with a solid horizontal line for ease of comparison.

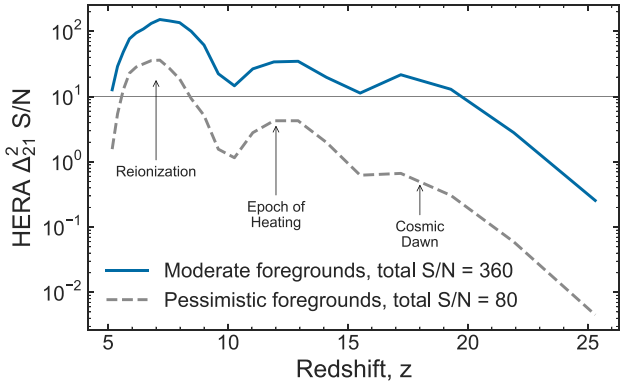


**Figure 5.** Signal-to-noise ratio of our fiducial EOS21 21-cm power spectrum as a function of redshift, using the moderate (blue solid) and pessimistic (grey dashed) expected noise from 1 yr of HERA data, as described in Section 2.4. Due to the frequency/redshift dependence of the noise, the pessimistic noise level would only enable high S/N measurements during the Epoch of Reionization, thus constraints on population III galaxies would be very limited, as seen in Fig. 3.

redshift bins corresponding to two adjacent HERA frequency 8 MHz bandwidths. From this figure, we see the lowest errors on population II parameters are obtained during the later stages of the Epoch of Reionization,  $z \sim 5-7$  (see Figs 6 and B1), when they strongly affect the 21-cm signal. At these redshifts, the observational noise is lowest (Fig. 5) and the redshift resolution due to our sampling of the light-cone in fixed frequency bins is highest, which will naturally increase the signal to noise for population II parameters. But by  $z \gtrsim 10$ , the errors on population II parameters become comparable to the errors on population III parameters, though the measurements are obtained in sparser redshift bins, and by  $z \gtrsim 15$  the errors on population III parameters are lower than the population II parameters – as lower

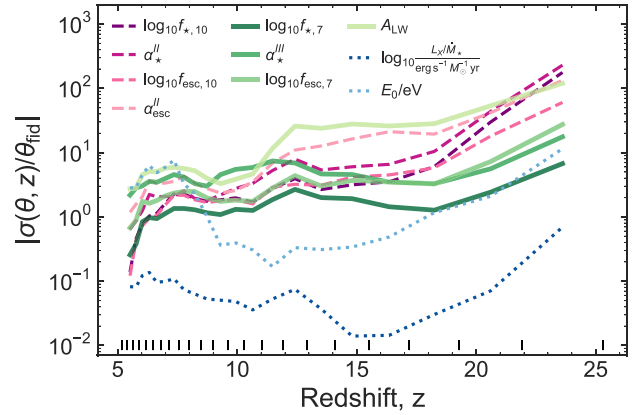


**Figure 6.** Fractional  $1\sigma$  error in each parameter as estimated from the Fisher matrix in rolling redshift bins corresponding to two adjacent HERA frequency channels, demonstrating the redshift evolution of measurable constraints on each parameter. All lines show the constraints using the moderate foreground noise model (see Section 2.4). Pink dashed lines show population II parameters, green solid lines show population III parameters, and blue dotted lines show X-ray parameters. Vertical black ticks show the redshift bin edges for our mock HERA observations.

mass galaxies start to dominate the star formation rate density and thus the 21-cm signal (e.g. see fig. 6 by Muñoz et al. 2022). Due to the wide frequency range of HERA, the redshift dependence of the uncertainties of the parameters is captured, thus the population III parameters can be well constrained. We can also see from fig. 6 that, as expected, the lowest errors on X-ray parameters are obtained during the Epoch of Heating ( $z \sim 10-18$  for the EOS21 model).

The Fisher forecast demonstrates there are strong degeneracies between the normalization and low-mass slope of the stellar-halo mass relation for both population II and III galaxies. There is also a very strong degeneracy between  $f_{*,10}^{\text{II}}$  and  $f_{\text{esc},10}^{\text{II}}$  as noted by Park et al. (2019).  $L_X/M_*$  is most strongly degenerate with population II parameters, but not as strongly with population III parameters. This stronger degeneracy is likely because population II galaxies are expected to dominate the star-formation rate density during the Epoch of Heating ( $z \lesssim 15$ , see e.g. Muñoz et al. 2022) and so the relative abundance of these galaxies is thus degenerate with their X-ray emission, whereas population III galaxies dominate the SFR density at higher redshifts, where X-ray heating has a smaller effect on the 21-cm signal.

In terms of an interplay between population II and III parameters, the strongest degeneracies are between  $f_{\text{esc},7}^{\text{III}}$  and population II parameters ( $\alpha_*^{\text{II}}$ ,  $f_{*,10}^{\text{II}}$ ,  $\alpha_{\text{esc}}$ ,  $f_{\text{esc},10}^{\text{II}}$ ), attributed to the uncertainty of the relative role of population III-hosting galaxies in reionization. Population III star formation parameters are also degenerate with  $A_{\text{LW}}$ , which is expected as it sets the strength of Lyman–Werner feedback which suppresses star formation in molecular cooling haloes.

We also produce forecasts for HERA observations adding a prior on  $\alpha_*^{\text{II}}$ . Park et al. (2019) demonstrated that adding other astrophysical observations to the 21-cm signal, in their case, the UV luminosity function (LF), provides independent constraints on the model parameters. In their case, they found uncertainties in population II star formation:  $f_{*,10}^{\text{II}}$  and  $\alpha_*^{\text{II}}$ , were reduced by a factor of three when adding UV LF data to their likelihood, as the UV LF provides important information to constrain the stellar-to-halo mass relation (equation 8). Here, we use the LF-only constraint

on  $\alpha_*^{\text{II}}$  inferred by Park et al. (2019) from *Hubble Space Telescope* observations,  $\sigma(\alpha_*^{\text{II}}) = 0.07$ , as a prior, by adding  $1/\sigma^2(\alpha_*^{\text{II}})$  to the diagonal element corresponding to  $\alpha_*^{\text{II}}$  in the Fisher matrix (e.g. Coe 2009). The impact on the total uncertainties in each parameter is shown in Fig. 4. Using the moderate foreground noise model, the impact of the  $\alpha_*^{\text{II}}$  prior is negligible, as population II parameters can already be measured to similar precision to the prior, but the prior significantly reduces uncertainties on population II parameters in the case of the pessimistic foreground noise.

Our forecasts demonstrate that observations of the 21-cm power spectrum could be able to determine the efficiency of both population II and population III star formation, if the foreground noise follows the ‘moderate’ prescription, and determine the strength of X-ray production by the first galaxies to sub- per cent precision even under ‘pessimistic’ noise. However, an understanding of the observational noise level is crucial. We note that although the ‘pessimistic’ foreground model is comparable to the noise model used by Park et al. (2019) our forecasted uncertainties for the EOS21 model can be higher because the fiducial parameters are different, and the increased number of free parameters adds additional uncertainty due to degeneracies between parameters.

### 3.3 Principal Components of the 21-cm power spectrum

Given the parametric model for galaxy formation in 21CMFAST, we may ask which combination of parameters can be best constrained by upcoming data. To obtain the most important linear combinations of parameters in the 21-cm signal, we carry out a principal component analysis of the Fisher matrix (e.g. Efstathiou 2002; Munshi & Kilbinger 2006).

To ensure all parameters are compared at approximately the same order of magnitude, we rescale  $E_0$  from eV to keV. Thus, we rescale the Fisher elements corresponding to  $E_0$  by a factor  $10^3$ .

We can diagonalize our adjusted Fisher matrix  $\mathcal{F}'$

$$\mathcal{F}' = \mathbf{U}\mathbf{\Lambda}\mathbf{U}^T \quad (18)$$

where  $\mathbf{\Lambda}$  is a diagonal matrix with elements  $\lambda_i$  and  $\mathbf{U}$  is the matrix of principal component eigenvectors, from which we can obtain the orthogonal linear combinations of the parameters  $\theta$

$$\mathbf{X} = \mathbf{U}^T\theta \quad (19)$$

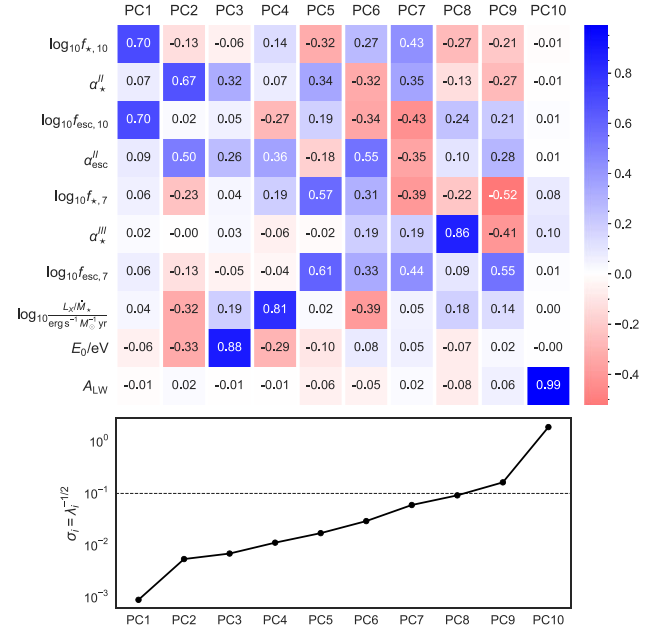
and the variance of the principal component (PC)  $X_i$  is  $1/\lambda_i$  (e.g. Efstathiou 2002).

Fig. 7 shows each PC and its associated uncertainty ( $\sigma_i = \lambda_i^{-1/2}$ ) as a function of the PC number  $i$ , in order of decreasing accuracy (lowest variance is the first PC). The first 7 out of 10 principal components can be measured to < 10 per cent accuracy, and only one, dominated by  $A_{\text{LW}}$ , to > 100 per cent.

These principal components demonstrate which combinations of parameters can be best constrained by HERA-like 21-cm power spectra. We obtain the principal components for the entire redshift range of HERA ( $z \sim 5-28$ ) and note that, the lowest variance components detectable in the full redshift range are mainly set by the frequency range with the lowest noise – i.e. the PCs that contribute the most at  $z \lesssim 8$  are heavily upweighted due to the much lower noise in that frequency range relative to the Cosmic Dawn window at  $z \gtrsim 12$ . We explore the PCs in a few redshift windows in Appendix B.

Several of the PCs have intuitive physical interpretations

(i) PC1 is dominated by  $f_{\star,10}^{\text{II}}$  and  $f_{\text{esc},10}^{\text{II}}$ . As these two quantities are constrained in log-space, this tells us that the product  $f_{\star,10}^{\text{II}} \times f_{\text{esc},10}^{\text{II}}$  will be well constrained by HERA. This is unsurprising as



**Figure 7.** (Upper) Eigenvectors associated with each principal component, in order of decreasing importance/increasing uncertainty. For example, PC1 is  $\approx f_{\text{esc},10}^{\text{II}} \times f_{\star,10}^{\text{II}}$ . (Lower) Uncertainty for each principal component.

this product determines the number of ionizing photons which are available for reionization and these quantities are very degenerate (see Fig. 3).

(ii) PC2 is dominated by a combination of population II and X-ray parameters, as these parameters have a strong impact on the signal during the Epoch of Reionization.

(iii) PC3 is dominated by  $E_0$ , which will be easily measured to high precision with minimal degeneracies with other parameters as it determines the hardness of the X-ray spectrum that emerges from early galaxies. Values of  $E_0$  below  $\sim 1$  keV have a strong impact on the inhomogeneity of X-ray heating (and thus the associated 21-cm power spectrum) since the mean free path is a strong function of the photon energy (e.g. Pacucci et al. 2014; Fialkov & Loeb 2016; Das et al. 2017).

(iv) PC4 is dominated by  $L_X/\dot{M}_*$ , which governs the relative timing of the X-ray heating epoch.

(v) Higher principal components have combinations of population II and population III parameters, with the combinations of population III parameters having the highest variance. As discussed in Appendix B, the principal components are dominated by which parameters can be measured in the redshift windows with lowest noise – thus when looking at the data over the full HERA observing window  $z \sim 5-28$  population II reionization parameters will be best measured.

(vi) PC10 is dominated by  $A_{\text{LW}}$ . As discussed in Section 3.2, this parameter is least constrained by 21-cm power spectra observations as it has a relatively low impact on the signal (see also fig. 17 by Muñoz et al. 2022).

We have tested the dependence of our results on the choice of fiducial model in Appendix A, where we use the EOS OPT model, which has an enhanced population III contribution to star formation and X-ray production (see Muñoz et al. 2022 for details). In the OPT model, we change the following parameters:  $f_{\star,10}^{\text{II}} = -1.25$ ,  $f_{\text{esc},10}^{\text{II}} = -1.2$ ,  $f_{\star,7}^{\text{III}} = -1.75$ ,  $f_{\text{esc},7}^{\text{III}} = -2.35$  and  $E_0 = 200$  eV. We find our

main results are unchanged: the product of  $f_{*,10}^{\text{II}} \times f_{\text{esc},10}^{\text{II}}$  is still the first principal component, the first four principal components are dominated by population II and X-ray parameters, and PC10 is dominated by  $A_{\text{LW}}$ .

### 3.4 Inference using the Fisher matrix

So far we have focused on the ability of the Fisher-matrix formalism to forecast errors with mock data. This can potentially save the running of computationally expensive MCMCs for enlarged parameter spaces (for instance, if new parameters such as ETHOS are included, Muñoz et al. 2020; Verwohlt et al. in preparation), and reuse the same Fisher matrix as above. However, the same formalism could be used for parameter inference from real data. We now explain the method for inference and its limitations.

The Fisher formalism assumes that the likelihood is Gaussian within the parameter range under consideration. For that, a requirement is that the observable ( $\Delta_{21}^2$ ) changes linearly with the parameters, i.e.  $\Delta_{21}^2(k, z) \approx \sum_i \theta_i f_i(k, z)$ , where  $f_i(k, z)$  are not necessarily linear. Under that assumption, we can infer shifts  $\delta\theta_i$  on parameters of a given data set, when compared to our fiducial (e.g. Muñoz et al. 2016). A major caveat is that this assumption of linearity is likely to break down when the observed parameters are a sufficient distance from the fiducial parameters.

We start by writing the observed 21-cm power spectrum as a linear function of the fiducial model power spectrum and the parameter shifts

$$\Delta_{21,\text{obs}}^2(k, z; \{\theta'\}) = \Delta_{21,\text{fid}}^2 + \sum_i \frac{\partial \Delta_{21,\text{fid}}^2}{\partial \theta_i} (\theta'_i - \theta_{i,\text{fid}}), \quad (20)$$

for a set of parameters  $\{\theta'\}$  which differ from the fiducial parameters,  $\{\theta_{\text{fid}}\}$ . This formula will be exact only for small parameter differences ( $\theta'_i - \theta_{i,\text{fid}} \ll 1$ ), but can allow us to quickly test the deviation between the parameters of an observation and those of our fiducial.

Given the difference  $\Delta_{21,\text{diff}}^2 = \Delta_{21,\text{obs}}^2(\theta') - \Delta_{21,\text{fid}}^2$  between the observed 21-cm PS with parameters  $\theta'$ , and that of the fiducial, we define the difference vector as

$$D_j = \sum_{i_k, i_z} \Delta_{21,\text{diff}}^2(k, z) \frac{\partial \Delta_{21,\text{fid}}^2(k, z)}{\partial \theta_j} \frac{1}{\sigma_{\Delta^2}^2(k, z)}, \quad (21)$$

akin to equation (16) (which defined the Fisher matrix), but with one of the derivatives swapped for  $\Delta_{21,\text{diff}}^2$ .

Then, taking into account the covariance matrix  $\mathcal{C} = \mathcal{F}^{-1}$  between parameters, we can find the shifts between the fiducial parameters and the observed ones as

$$\delta\theta_i = \theta'_i - \theta_{i,\text{fid}} = \sum_j \mathcal{C}_{ij} D_j. \quad (22)$$

We test this formalism by comparing two different choices of mock observations against our baseline (EOS21) fiducial one.

(i) In the first, we only slightly modified the parameters, randomly sampling the parameters from within  $1\sigma$  of our expected errors for the EOS fiducial with moderate noise (i.e. they fall within the blue ellipses in Fig. 3). In this case, we expect the likelihood to be roughly Gaussian, and the shifts to be consistent with the inputs.

(ii) In the second, we aim to infer the OPT EOS model, which has an enhanced population III contribution to star formation and X-ray production (see Muñoz et al. 2022 for details). In the OPT model, we change the following parameters:  $f_{*,10}^{\text{II}} = -1.25$ ,  $f_{\text{esc},10}^{\text{II}} = -1.2$ ,  $f_{*,7}^{\text{III}} = -1.75$ ,  $f_{\text{esc},7}^{\text{III}} = -2.35$  and  $E_0 = 200$  eV. These are

significantly different from our EOS21 fiducial (see Table 1), so they will test how far from the fiducial the parameters can be before the formalism breaks down.

In both cases, we generate the new mock observed 21-cm power spectra,  $\Delta_{21,\text{obs}}^2(\theta')$ , using identical settings as for our fiducial EOS run, changing only the astrophysical parameters.

A subtlety in this analysis is that, as well as the Poisson noise in the power spectrum – due to measuring the power spectrum from a finite number of  $k$ -space modes in the simulation boxes – both our fiducial and ‘observed’ mocks have sample (cosmic) variance as they are each independent realizations of the initial conditions. Both the Poisson noise and cosmic variance depend on the volume of the simulations (see e.g. Iliev et al. 2014; Kaur et al. 2020 for the power spectrum and Muñoz & Cyr-Racine 2021 for the global signal). Thus, the total noise on the power spectrum is the Poisson, cosmic variance and instrumental noise terms added in quadrature:  $\sigma_{\text{tot}}^2(k, z) = \sigma_{\text{poiss.}}^2(k, z) + \sigma_{\text{c.v.}}^2(k, z) + \sigma_{\text{instr.}}^2(k, z)$ . As such, using the Fisher matrix as defined above undercounts the error bars on our mock observation, as we have assumed the mock has the cosmic variance from a HERA-like cosmic observation (approximately 150 Gpc<sup>3</sup>; DeBoer et al. 2017), rather than the much smaller volume of our mock simulation (0.064 Gpc<sup>3</sup>, see Section 2.4).

To circumvent the issue of cosmic variance, we first run the two cases with the same initial conditions as our EOS fiducial. Using simulations with the same initial conditions as the fiducial, we find that we can recover the ‘observed’ parameters within  $2\sigma$  (7/10 parameters recovered within  $1\sigma$ ) for case (i), but the inferred parameters are not well recovered for case (ii), with only 1/10 parameters recovered within  $1\sigma$ . The biggest offset between the inferred and true values are for parameters where the shift  $\delta\theta_i$  is greater than the  $1\sigma$  errors on the fiducial value. We surmise that the inference approach outlined above only works well when the assumption that the power spectrum varies linearly with the parameters holds – i.e. when the likelihood is most like a Gaussian, and the ‘true’ parameters are within  $1\sigma$  of the peak likelihood for our specific fiducial.

When varying the initial conditions, we find a worse recovery of the parameter shifts for both cases. This is ameliorated when increasing the instrumental error bars (using our ‘pessimistic’ noise case), as that increases the variance of each  $k$  number, which partially accounts for the undercounted cosmic variance. Given that we cannot ‘match’ the initial conditions of a real power spectrum detection in the sky, we conclude that using the Fisher matrix for inference is challenging in our formalism, even if the likelihood is approximately Gaussian. Thus a dedicated variance analysis may be required but is beyond the scope of this paper. We note that as our simulation volumes are converged for the power spectrum on the scales we consider (see Section 2.4 and e.g. Kaur et al. 2020), the cosmic variance noise should be subdominant to other sources of noise. Thus, the poor performance of the Fisher matrix inference is likely dominated by the non-linearity of the power spectrum as a function of the parameters.

## 4 DISCUSSION

### 4.1 Computational efficiency

The key advantage of using Fisher matrices over MCMC is the reduced computational time, due to requiring far fewer individual simulation runs. For the Fisher-matrix calculation, we require  $2N + 1$  simulations, where  $N$  is the number of free parameters, whereas

for an MCMC with 21CMC of order  $\sim 10^5$  simulations are required to reach convergence (Greig & Mesinger 2017).

For comparison, the MCMC run by Park et al. (2019) required 70 000 individual simulations, including burn-in steps, whereas our Fisher-matrix calculation using the same fiducial parameters required only 17 individual simulations. While the simulation generation can be parallelized, we still expect the Fisher-matrix approach can greatly reduce the computation time compared to an MCMC. The Fisher matrix also has the advantage that additional parameters can be varied by just running a couple of new simulations, rather than having to rerun an MCMC to explore the joint posterior. While an MCMC should be the gold standard for analysis of observations (e.g. Ghara et al. 2020, 2021; Greig et al. 2021a, b; The HERA Collaboration et al. 2022a, 2023), we have demonstrated that a Fisher-matrix analysis can accurately recover the same parameter degeneracies and uncertainties.

This means a Fisher-matrix approach could be useful for testing and prototyping analyses to forecast parameter uncertainties. Potential applications could be: adding new parameters – for example cosmological and dark-matter parameters, which will be the topic of a future work (Verwohlt et al. in preparation); or testing the impact of instrument/observing designs (described more below).

The limitations of the Fisher-matrix approach are that, as described in Section 3.4, it is difficult to use the Fisher-matrix approach for actual inference, thus MCMC or nested sampling will still be required to map full posterior when we have 21-cm observations. But, for forecasting, the Fisher-matrix approach is extremely efficient for estimating parameter uncertainties assuming a fiducial model (e.g. using the maximum *a posteriori* model from current, non-21-cm observations (e.g. Park et al. 2019; Qin et al. 2021b). Additionally, parameter estimates from Fisher matrices are always optimistic, as the Fisher matrix will always produce the lower bound on the possible observed covariance matrix due to the assumption of a multivariate Gaussian posterior (see Section 2.3), so it is possible that some of the uncertainties will be underestimated.

## 4.2 Importance of understanding observational noise

As demonstrated in Section 3.2, assumptions about the noise level of the 21-cm observations can have order of magnitude effects on the inferred parameter constraints. Fig. 4 shows the fractional error in each parameter under the assumption of the moderate and pessimistic foreground noise models, with and without the inclusion of the UV LF prior on  $\alpha_{*}^{\text{II}}$ .

An advantage of the Fisher-matrix approach is that it is very efficient to rerun the forecast analysis under different assumptions of the foreground noise model, whereas using an MCMC, this would require recalculating the likelihood for every simulation. As a good understanding of the noise is crucial to measuring astrophysics and cosmology from 21-cm observations, our approach provides an efficient way to assess the impact of assumptions in instrumental noise and foreground models.

## 5 CONCLUSIONS

We have created a Fisher-matrix wrapper for the public code 21CMFAST, 21CMFISH, enabling rapid parameter forecasts from the cosmic 21-cm signal. Our conclusions are as follows

(i) We verify that our Fisher-matrix analysis recovers the same parameter degeneracies and produces comparable uncertainties as the 21cm-only MCMC of Park et al. (2019), requiring only  $\sim$

0.03 per cent of the individual simulations. This means that, under the assumption of a multivariate Gaussian posterior, a Fisher matrix can be used to rapidly explore parameter constraints with 21-cm observations (see also e.g. Pober et al. 2014; Liu & Parsons 2016; Shimabukuro et al. 2017; Muñoz et al. 2020; Jones et al. 2021), significantly reducing the requirement for expensive and energy intensive computation when prototyping analyses (and does not require training, cf. emulator approaches e.g. Kern et al. 2017).

(ii) Using our Fisher-matrix approach, we perform the first joint analysis of population II and population III galaxy parameters as well as those characterizing feedback from radiative backgrounds. We find that under the assumption of a ‘moderate’ foreground noise floor (using the ‘moderate’ foregrounds model in 21CMSENSE, with a superhorizon buffer  $a = 0.1 h \text{ Mpc}^{-1}$  and expected HERA system temperature; DeBoer et al. 2017), both population II and population III parameters can be constrained by future HERA data to  $\lesssim 10$  per cent precision, due to the relative importance of the parameters as a function of redshift and the wide frequency coverage of HERA.

(iii) Adding priors on parameters from independent measurements of the UV luminosity function from HUBBLE SPACE TELESCOPE data to 21-cm observations improves constraints on population II parameters by approximately a factor of three in the case of pessimistic foreground noise, but does not significantly improve estimates in the case of moderate foreground noise as those constraints are already comparable to the UV LF information.

(iv) A principal component analysis demonstrates that at least 7 combinations of the parameters could be well measured by HERA. The first four principal components are dominated by  $f_{\text{esc},10}^{\text{II}}, f_{*10}^{\text{II}}$  and combinations of population II and X-ray emission properties, as these are the most important features in determining the strength of the 21-cm signal at  $z \lesssim 10$  where the signal will be best measured. Our analysis shows the ionizing photon escape fraction and stellar-to-halo mass fraction are highly degenerate using 21-cm observations alone (see also Park et al. 2019).

(v) We attempt to use our Fisher-matrix approach to perform an inference of simulated data and find that it is only possible to reliably recover parameters that were within  $1\sigma$  of the fiducial simulation and when using the same initial conditions for the fiducial and mock data simulations. Thus, we caution that while the Fisher matrix is useful for forecasting, within our formalism, it is not a good choice for inference: Bayesian inference techniques such as MCMC or Nested sampling are more appropriate for mapping out the full posterior for unknown parameters, once detections are available.

Our results show that Fisher-matrix analyses provide a fast and realistic way to estimate parameter uncertainties from future 21-cm observations, under the assumption the posterior is a multivariate Gaussian and also assuming the noise is separable from the cosmic signal. This greatly reduces the requirement for expensive MCMC runs when prototyping new analyses or adding additional parameters. This framework enables us to more easily explore the effects of foreground noise and the degeneracies between astrophysical and cosmological, e.g. dark-matter, parameters, which will be the topic of a future work.

## SOFTWARE

21CMFAST (Mesinger et al. 2011; Park et al. 2019; Murray et al. 2020; Qin et al. 2020; Muñoz et al. 2022), 21CMSENSE (Pober et al. 2014), CORNER (Foreman-Mackey 2016), IPYTHON (Pérez & Granger 2007), MATPLOTLIB (Hunter 2007), NUMPY (Van Der Walt, Colbert &

Varoquaux 2011), SCIPY (Oliphant 2007), ASTROPY (Robitaille et al. 2013).

## ACKNOWLEDGEMENTS

CAM acknowledges support by the VILLUM FONDEN under grant 37459, the Carlsberg Foundation under grant CF22-1322, and from NASA Headquarters through the NASA Hubble Fellowship grant HST-HF2-51413.001-A awarded by the Space Telescope Science Institute, which is operated by the Association of Universities for Research in Astronomy, Inc., for NASA, under contract NAS5-26555. The Cosmic Dawn Center (DAWN) is funded by the Danish National Research Foundation under grant DNR140. JBM acknowledges support by a Clay Fellowship at the Smithsonian Astrophysical Observatory. Parts of this research were supported by the Australian Research Council Centre of Excellence for All Sky Astrophysics in 3 Dimensions (ASTRO 3D), through project number CE170100013. JP was supported by a KIAS individual Grant (PG078701) at Korea Institute for Advanced Study.

## DATA AVAILABILITY

Our Fisher analysis package for 21CMFAST is available in a public python package 21CMFISH: <https://github.com/charlottenosam/21cmfish>. The code and accompanying data to reproduce plots in this paper are included in the package.

## REFERENCES

- Albrecht A. et al., 2009, preprint (arXiv:0901.0721)
- Barkana R., Loeb A., 2001, *Phys. Rep.*, 349, 125
- Barkana R., Loeb A., 2005, *ApJ*, 626, 1
- Battaglia N., Trac H., Cen R., Loeb A., 2013, *ApJ*, 776, 81
- Behroozi P. S., Silk J., 2015, *ApJ*, 799, 32
- Behroozi P. S., Marchesini D., Wechsler R. H., Muzzin A., Papovich C., Stefanon M., 2013, *ApJ*, 777, L10
- Bosman S. E. I., Fan X., Jiang L., Reed S., Matsuoka Y., Becker G., Haehnelt M., 2018, *MNRAS*, 479, 1055
- Bouwens R. J. et al., 2015, *ApJ*, 803, 34
- Bowman J. D., Rogers A. E. E., Monsalve R. A., Mozdzen T. J., Mahesh N., 2018, *Nature*, 555, 67
- Choudhury T. R., Paranjape A., 2018, *MNRAS*, 481, 3821
- Coe D., 2009, preprint (arXiv:0906.4123)
- Das A., Mesinger A., Pallottini A., Ferrara A., Wise J. H., 2017, *MNRAS*, 469, 1166
- Davies F. B., Becker G. D., Furlanetto S. R., 2018, *ApJ*, 860, 155
- DeBoer D. R. et al., 2017, *PASP*, 129, 045001
- Efstathiou G., 2002, *MNRAS*, 332, 193
- Ewall-Wice A., Hewitt J., Mesinger A., Dillon J. S., Liu A., Pober J., 2016, *MNRAS*, 458, 2710
- Fialkov A., Loeb A., 2016, *ApJ*, 821, 59
- Fialkov A., Barkana R., Visbal E., Tseliakhovich D., Hirata C. M., 2013, *MNRAS*, 432, 2909
- Foreman-Mackey D., 2016, *J. Open Source Softw.*, 1, 24
- Fragos T., Lehmer B. D., Naoz S., Zezas A., Basu-Zych A., 2013, *ApJ*, 776, L31
- Furlanetto S. R., 2006, *MNRAS*, 371, 867
- Furlanetto S. R., Oh S. P., Briggs F. H., 2006, *Phys. Rep.*, 433, 181
- Gehlot B. K. et al., 2019, *MNRAS*, 488, 4271
- Ghara R., Choudhury T. R., Datta K. K., 2015, *MNRAS*, 447, 1806
- Ghara R. et al., 2020, *MNRAS*, 493, 4728
- Ghara R., Giri S. K., Ciardi B., Mellema G., Zaroubi S., 2021, *MNRAS*, 503, 4551
- Greig B., Mesinger A., 2015, *MNRAS*, 449, 4246
- Greig B., Mesinger A., 2017, *MNRAS*, 472, 2651
- Greig B., Mesinger A., 2018, *MNRAS*, 477, 3217
- Greig B., Mesinger A., Haiman Z., Simcoe R. A., 2017, *MNRAS*, 466, 4239
- Greig B., Mesinger A., Bañados E., 2019, *MNRAS*, 484, 5094
- Greig B., Trott C. M., Barry N., Mutch S. J., Pindor B., Webster R. L., Wyithe J. S. B., 2021a, *MNRAS*, 500, 5322
- Greig B. et al., 2021b, *MNRAS*, 501, 1
- Greig B., Ting Y.-S., Kurov A. A., 2022, *MNRAS*, 513, 1719
- Hills R., Kulkarni G., Meerburg P. D., Puchwein E., 2018, *Nature*, 564, E32
- Hirata C. M., 2006, *MNRAS*, 367, 259
- Hoag A. et al., 2019, *ApJ*, 878, 12
- Hunter J. D., 2007, *Comput. Sci. Eng.*, 9, 99
- Hutter A., Dayal P., Yepes G., Gottlöber S., Legrand L., Ucci G., 2021, *MNRAS*, 503, 3698
- Iliev I. T., Mellema G., Ahn K., Shapiro P. R., Mao Y., Pen U. L., 2014, *MNRAS*, 439, 725
- Jones D., Palatnick S., Chen R., Beane A., Lidz A., 2021, *ApJ*, 913, 7
- Kaur H. D., Gillet N., Mesinger A., 2020, *MNRAS*, 495, 2354
- Kern N. S., Liu A., Parsons A. R., Mesinger A., Greig B., 2017, *ApJ*, 848, 23
- Koopmans L. et al., 2015, preprint (arXiv:1505.07568)
- Kulkarni M., Visbal E., Bryan G. L., 2021, *ApJ*, 917, 40
- Liu A., Parsons A. R., 2016, *MNRAS*, 457, 1864
- Liu A., Shaw J. R., 2020, *PASP*, 132, 062001
- Liu A., Tegmark M., Bowman J., Hewitt J., Zaldarriaga M., 2009, *MNRAS*, 398, 401
- Liu A., Pritchard J. R., Tegmark M., Loeb A., 2013, *Phys. Rev. D*, 87, 043002
- Loeb A., Zaldarriaga M., 2004, *Phys. Rev. Lett.*, 92, 211301
- Machacek M. E., Bryan G. L., Abel T., 2001, *ApJ*, 548, 509
- Majumdar S., Mellema G., Datta K. K., Jensen H., Choudhury T. R., Bharadwaj S., Friedrich M. M., 2014, *MNRAS*, 443, 2843
- Mason C. A., Trenti M., Treu T., 2015, *ApJ*, 813, 21
- Mason C. A., Treu T., Dijkstra M., Mesinger A., Trenti M., Pentericci L., de Barros S., Vanzella E., 2018, *ApJ*, 856, 2
- Mason C. A. et al., 2019, *MNRAS*, 485, 3947
- McGreer I. D., Mesinger A., D’Odorico V., 2015, *MNRAS*, 447, 499
- McQuinn M., 2012, *MNRAS*, 426, 1349
- Mertens F. G. et al., 2020, *MNRAS*, 493, 1662
- Mesinger A., 2019, *The Cosmic 21-cm Revolution; Charting the first billion years of our universe*, IOP Publishing, IOP Publishing
- Mesinger A., Furlanetto S., 2007, *ApJ*, 669, 663
- Mesinger A., Furlanetto S., Cen R., 2011, *MNRAS*, 411, 955
- Mineo S., Gilfanov M., Sunyaev R., 2011, *Astron. Nachr.*, 332, 349
- Mirocha J., 2014, *MNRAS*, 443, 1211
- Mondal R., Bharadwaj S., Majumdar S., 2017, *MNRAS*, 464, 2992
- Morales M. F., Wyithe J. S. B., 2010, *ARA&A*, 48, 127
- Morales A. M., Mason C. A., Bruton S., Gronke M., Haardt F., Scarlata C., 2021, *ApJ*, 919, 120
- Moster B. P., Naab T., White S. D. M., 2013, *MNRAS*, 428, 3121
- Muñoz J. B., 2019a, *Phys. Rev. D*, 100, 063538
- Muñoz J. B., 2019b, *Phys. Rev. Lett.*, 123, 131301
- Muñoz J. B., Cyr-Racine F.-Y., 2021, *Phys. Rev. D*, 103, 023512
- Muñoz J. B., Grin D., Dai L., Kamionkowski M., Kovetz E. D., 2016, *Phys. Rev. D*, 93, 043008
- Muñoz J. B., Dvorkin C., Cyr-Racine F.-Y., 2020, *Phys. Rev. D*, 101, 063526
- Muñoz J. B., Qin Y., Mesinger A., Murray S. G., Greig B., Mason C., 2022, *MNRAS*, 511, 3657
- Munshi D., Kilbinger M., 2006, *A&A*, 452, 63
- Murray S. G., Greig B., Mesinger A., Muñoz J. B., Qin Y., Park J., Watkinson C. A., 2020, *J. Open Source Software*, 5, 2582
- Mutch S. J., Geil P. M., Poole G. B., Angel P. W., Duffy A. R., Mesinger A., Wyithe J. S. B., 2016, *MNRAS*, 462, 250
- Oh S. P., Haiman Z., 2002, *ApJ*, 569, 558
- Oliphant T. E., 2007, *Comput. Sci. Eng.*, 9, 10
- Ouchi M. et al., 2010, *ApJ*, 723, 869
- Pacucci F., Mesinger A., Mineo S., Ferrara A., 2014, *MNRAS*, 443, 678
- Park J., Mesinger A., Greig B., Gillet N., 2019, *MNRAS*, 484, 933
- Pérez F., Granger B. E., 2007, *Comput. Sci. Eng.*, 9, 21
- Planck Collaboration XLVII, 2016, *A&A*, 596, A108
- Planck Collaboration VI, 2020, *A&A*, 641, A6

- Pober J. C. et al., 2013, *ApJ*, 768, L36  
Pober J. C. et al., 2014, *ApJ*, 782, 66  
Pritchard J. R., Loeb A., 2012, *Rep. Prog. Phys.*, 75, 086901  
Qin Y., Mesinger A., Park J., Greig B., Muñoz J. B., 2020, *MNRAS*, 495, 123  
Qin Y., Mesinger A., Greig B., Park J., 2021a, *MNRAS*, 501, 4748  
Qin Y., Mesinger A., Bosman S. E. I., Viel M., 2021b, *MNRAS*, 506, 2390  
Robitaille T. P. et al., 2013, *A&A*, 558, A33  
Sabti N., Muñoz J. B., Blas D., 2022a, *Phys. Rev. D*, 105, 043518  
Sabti N., Muñoz J. B., Blas D., 2022b, *ApJ*, 928, L20  
Santos M. G., Ferramacho L., Silva M. B., Amblard A., Cooray A., 2010, *MNRAS*, 406, 2421  
Schauer A. T. P., Glover S. C. O., Klessen R. S., Clark P., 2021, *MNRAS*, 507, 1775  
Shaw A. K., Bharadwaj S., Mondal R., 2020, *MNRAS*, 498, 1480  
Sheth R. K., Mo H. J., Tormen G., 2001, *MNRAS*, 323, 1  
Shimabukuro H., Yoshiura S., Takahashi K., Yokoyama S., Ichiki K., 2017, *MNRAS*, 468, 1542  
Singh S. et al., 2022, *Nat. Astron.*, 6, 607  
Sitwell M., Mesinger A., Ma Y.-Z., Sigurdson K., 2014, *MNRAS*, 438, 2664  
Skinner D., Wise J. H., 2020, *MNRAS*, 492, 4386  
Sobacchi E., Mesinger A., 2014, *MNRAS*, 440, 1662  
Sobacchi E., Mesinger A., 2015, *MNRAS*, 453, 1843  
Sun G., Furlanetto S. R., 2016, *MNRAS*, 460, 417  
Taccella S., Bose S., Conroy C., Eisenstein D. J., Johnson B. D., 2018, *ApJ*, 868, 92  
The HERA Collaboration et al., 2023, *ApJ*, 945, 124  
The HERA Collaboration et al., 2022b, *ApJ*, 924, 51  
The HERA Collaboration et al., 2022c, *ApJ*, 925, 221  
Tingay S. J. et al., 2013, *PASA*, 30, e007  
Trott C. M. et al., 2020, *MNRAS*, 493, 4711  
Trotta R., 2008, *Contemp. Phys.*, 49, 71  
Tseliakhovich D., Hirata C., 2010, *Phys. Rev. D*, 82, 083520  
Van Der Walt S., Colbert S. C., Varoquaux G., 2011, *Comput. Sci. Eng.*, 13, 22  
Visbal E., Loeb A., 2010, *J. Cosmology Astropart. Phys.*, 2010, 016  
Visbal E., Haiman Z., Terrazas B., Bryan G. L., Barkana R., 2014, *MNRAS*, 445, 107  
Wang F. et al., 2020, *ApJ*, 896, 23  
Whitler L. R., Mason C. A., Ren K., Dijkstra M., Mesinger A., Pentericci L., Trenti M., Treu T., 2020, *MNRAS*, 495, 3602  
Yung L. Y. A., Somerville R. S., Finkelstein S. L., Popping G., Davé R., Venkatesan A., Behroozi P., Ferguson H. C., 2020, *MNRAS*, 496, 4574  
van Haarlem M. P. et al., 2013, *A&A*, 556, A2

## APPENDIX A: DEPENDENCE ON CHOICE OF FIDUCIAL MODEL

We do not know the model that best describes the data *a priori*. In the above, we have used a fiducial model which uses constraints from existing observations (e.g. the cosmic SFR density and the reionization timeline) to inform the astrophysical parameters of our model. The exact precision with which we can measure astrophysical parameters (Section 3.2) and the combination of parameters which

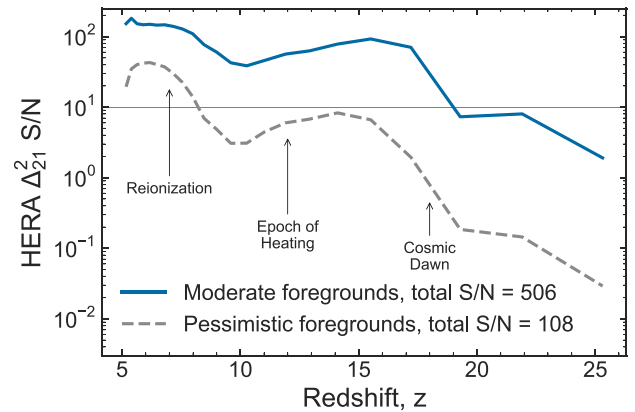


Figure A1. Same as Fig. 5 but for the EOS OPT fiducial model.

can be best constrained (Section 3.3) will depend on the fiducial model, as the relative strength of the population II and III galaxy components and of X-ray heating will all change the 21-cm signal. However, because these effects change the signal in different ways (as demonstrated by our PCA analysis in Section 3.3), we expect our results will not be strongly affected qualitatively by the choice of fiducial model.

To assess this in more detail, we carry out the same analysis as in Sections 3.2 and 3.3 for a second fiducial model, the EOS OPT model (also used in Section 3.4, see Muñoz et al. 2022) which has an enhanced contribution of population III galaxies to star formation and enhanced X-ray emission compared to our original model. In the OPT model, we change the following parameters:  $f_{\star,10}^{\text{II}} = -1.25$ ,  $f_{\text{esc},10}^{\text{II}} = -1.2$ ,  $f_{\star,7}^{\text{III}} = -1.75$ ,  $f_{\text{esc},7}^{\text{II}} = -2.35$  and  $E_0 = 200$  eV. We find our results are qualitatively unchanged.

We show the signal-to-noise ratio of this 21-cm power spectrum in Fig. A1, where we see an increased S/N, particularly during the Epoch of Heating due to the higher X-ray heating, compared to our EOS fiducial model (Fig. 5). The parameter constraint forecast is plotted in Fig. A2 and the fractional error on each parameter in Fig. A3. Because the S/N ratio is higher for this model, we find less of a difference between the moderate and pessimistic foregrounds. Because of the increased population III galaxy contribution to the cosmic SFR density, we find population III galaxy parameters could be slightly better constrained than in our original fiducial, while population II galaxy parameters would be slightly less well constrained because there are degeneracies between parameters governing the two galaxy populations

Finally, we show the principal components of the 21-cm power spectrum in Fig. A4. The principal components are very similar to those of the EOS model (Fig. 7). The product of  $f_{\star,10}^{\text{II}} \times f_{\text{esc},10}^{\text{II}}$  is still the first principal component, the first four principal components are dominated by population II and X-ray parameters (with X-ray parameters contributing slightly more to the PCs compared to in the EOS model), and  $A_{1W}$  is still the last principal component.

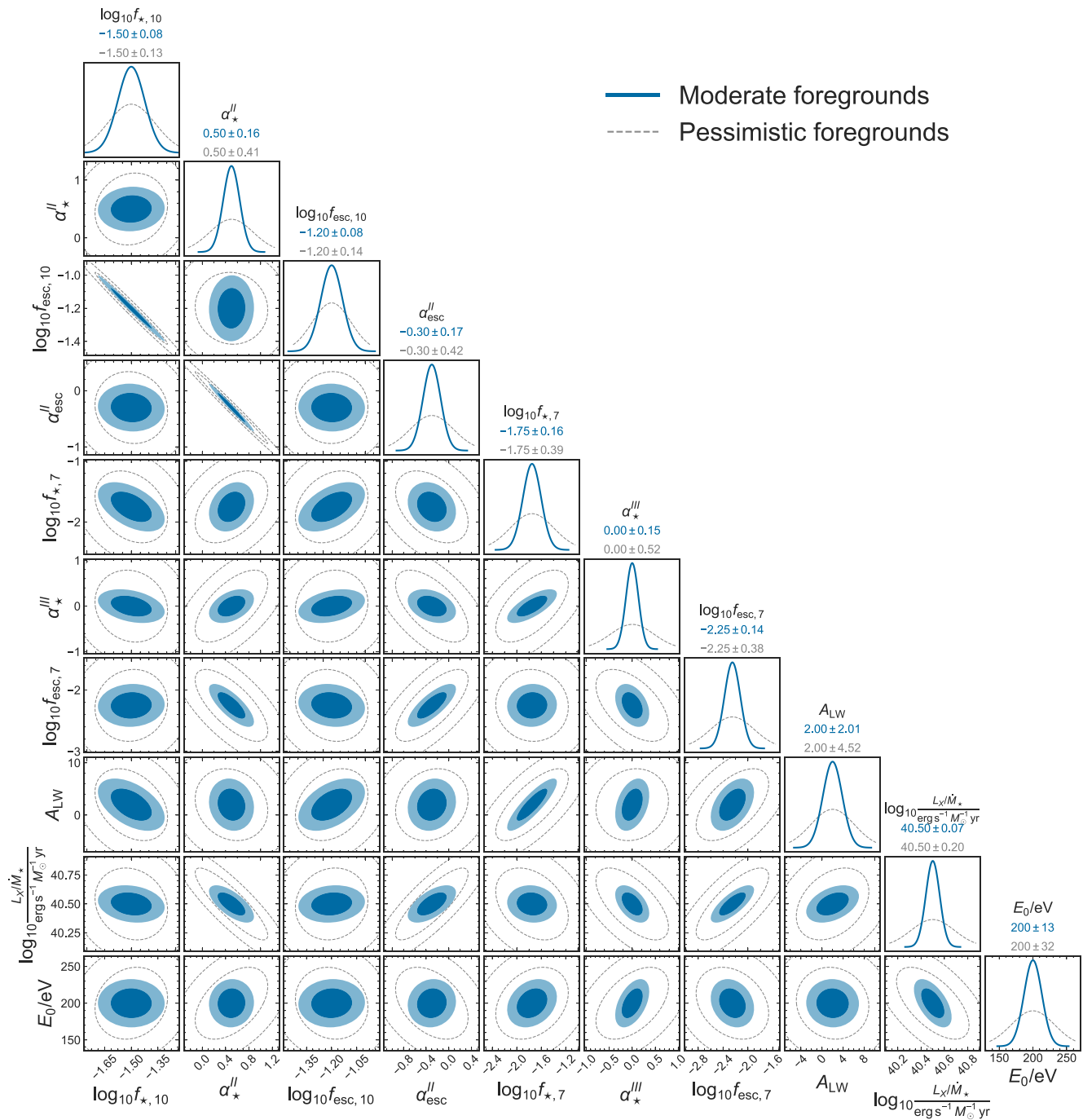


**Figure A2.** Same as Fig. 3 but for the EOS OPT fiducial model.

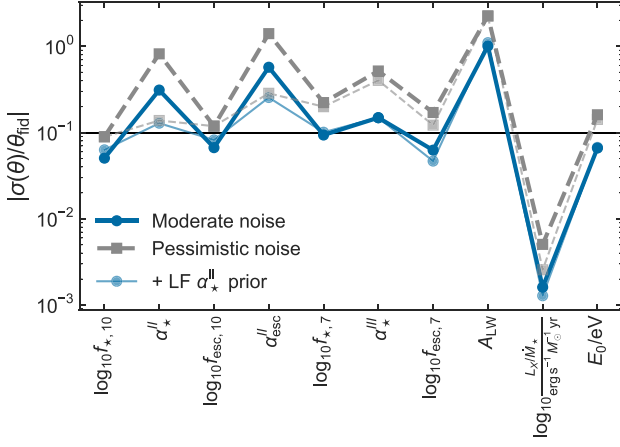


**Figure A3.** Same as Fig. 4 but for the EOS OPT fiducial model.

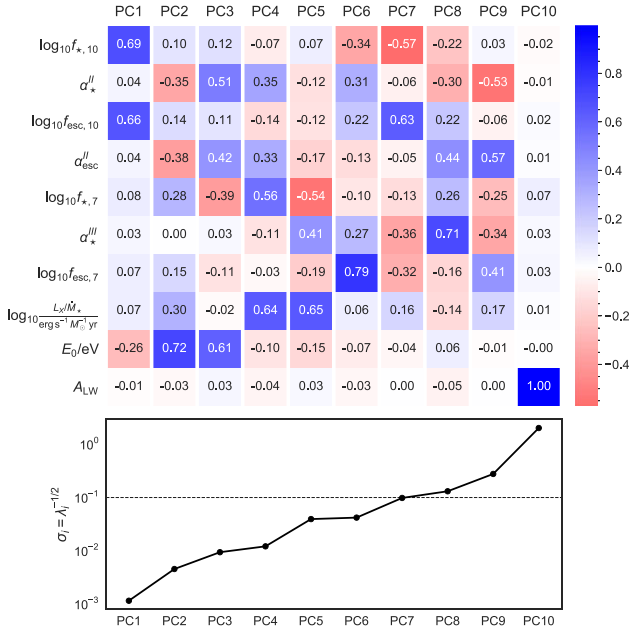


**Figure A4.** Same as Fig. 7 but for the EOS OPT fiducial model.

## APPENDIX B: PRINCIPAL COMPONENT ANALYSIS IN REDSHIFT WINDOWS

Our principal component analysis in Section 3.3 demonstrates the combinations of parameters that will be best constrained by the full HERA data set. However, due to the strong frequency and therefore redshift dependence of the noise (see Fig. 5), where the background is higher at lower frequencies (e.g. DeBoer et al. 2017), the principal components are dominated by the parameters most important for the Epoch of Reionization – at  $z \lesssim 10$  where the noise is lowest.

To provide more insight into the redshift dependence of the principal components, we do a PCA in three redshift bins, corresponding to: the Epoch of Reionization ( $z \sim 5-10$ ), where the global 21-cm signal peaks and declines to zero); the Epoch of Heating ( $z \sim 10-15$ ), the signal goes from absorption to emission as the IGM is heated (likely by X-ray emission from the first galaxies); and early Cosmic Dawn ( $z \sim 15-30$ ), where the global signal starts to drop due to feedback from the first stars, until it reaches the trough before heating dominates.

We plot the principal components from these three redshift bins in Fig. B1. These plots demonstrate which combinations of parameters the observed redshift windows are most sensitive to. For the Reionization redshift window, we see the first principal component is very similar to the one obtain for the whole redshift range:  $f_{*,10}^{II} \times f_{esc,10}^{II}$ . The following principal components are dominated by population II and X-ray parameters, as expected during the Reionization epoch. In the Epoch of Heating, the primary principal components are dominated by X-ray parameters, as expected, as in the model, X-rays are the dominant driver of IGM heating. For the Cosmic Dawn redshift window, the first principal components are dominated by X-ray parameters and a combination of population III parameters.

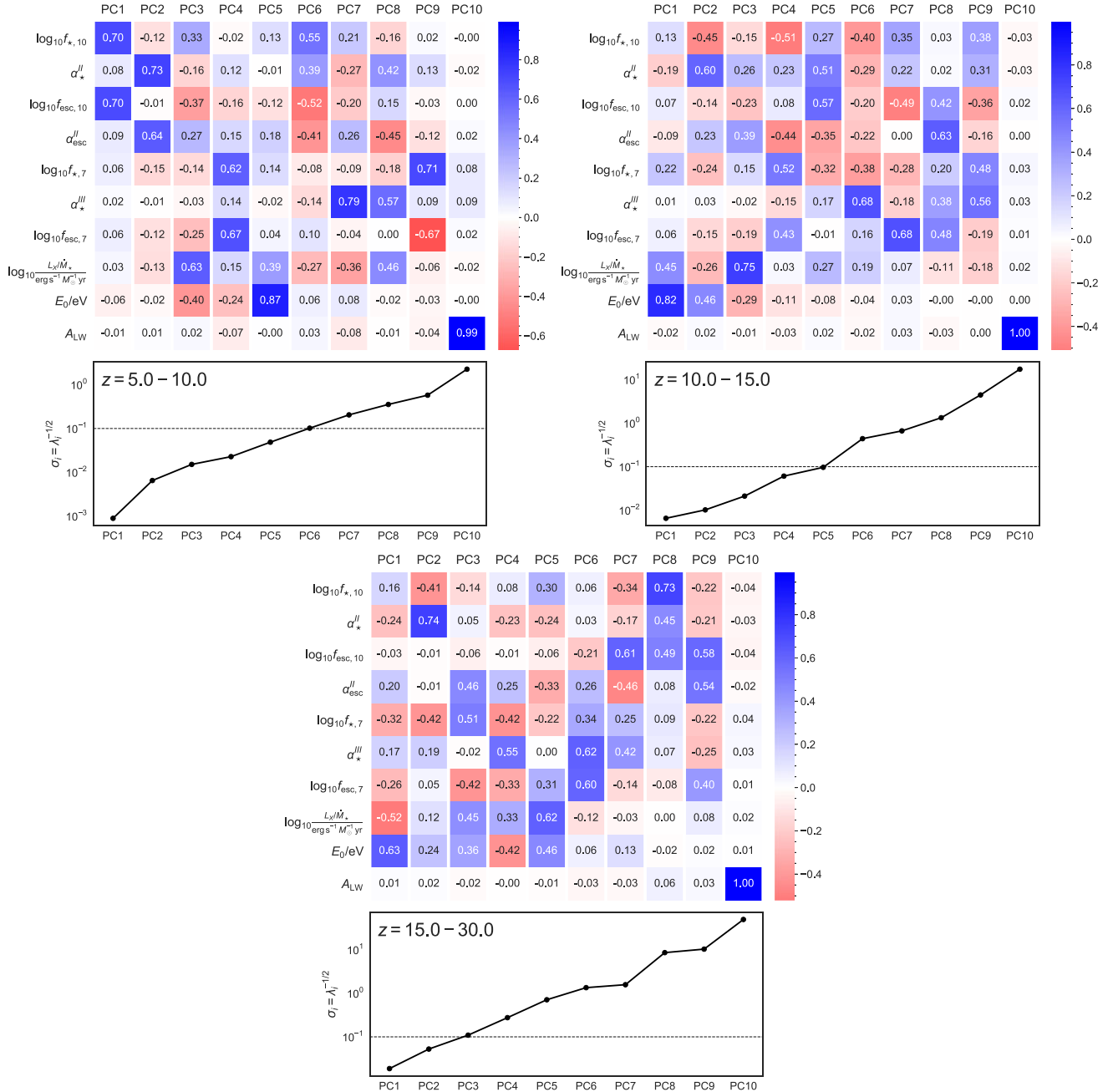


**Figure B1.** (Upper Left) Eigenvectors associated with each principal component, in order of decreasing importance/increasing uncertainty, in the Epoch of Reionization redshift window  $z \sim 5-10$ . (Upper Right) Eigenvectors associated with each principal component, in order of decreasing importance/increasing uncertainty, in the Epoch of Heating redshift window  $z \sim 10-15$ . (Lower) Eigenvectors associated with each principal component, in order of decreasing importance/increasing uncertainty, in the early Cosmic Dawn redshift window  $z \sim 15-30$ .

This paper has been typeset from a  $\text{\TeX/L\AA\TeX}$  file prepared by the author.